

# Search for Spatially Extended *Fermi*-LAT Sources Using Two Years of Flight Data

J. Lande<sup>2</sup>, S. Funk<sup>2</sup>, M. Ackermann (???), A. Allafort<sup>2</sup>, K. Bechtol<sup>2</sup>, M.-H. Grondin<sup>53</sup>, ...

## ABSTRACT

We present a new method for quantifying the spatial extension of sources with the Large Area Telescope (LAT), the primary science instrument on the *Fermi Gamma-ray Space Telescope* (*Fermi*). Spatial extension is an important characteristic for correctly associating LAT sources with their counterparts at other wavelengths. We perform a series of Monte Carlo studies to validate this tool and calculate the LAT's threshold for detecting the spatial extension of sources. We then use this tool to test all sources in the two year source catalog for extension. We report the detection of nine spatially extended sources in addition to the twelve spatially extended sources reported in the second *Fermi*-LAT Catalog (2FGL).

*Subject headings:* Catalogs; Fermi Gamma-ray Space Telescope; Gamma rays: observations; ISM: supernova remnants; Methods: statistical; pulsar wind nebula

## 1. Introduction

The Large Area Telescope (LAT) is a pair conversion telescope on the *Fermi Gamma-ray Space Telescope* (*Fermi*) that been surveying the  $\gamma$ -ray sky since 2008 June. The LAT has broad energy coverage (20 MeV to  $> 300$  GeV), wide field of view ( $\sim 2.4$ sr), and large effective area ( $\sim 8000$  cm<sup>2</sup> at  $> 1$ GeV).

Using two years of all-sky surveying data, the LAT Collaboration published a catalog of 1873 GeV sources (Abdo et al. 2011b). Many of these have been positionally associated with a variety of source classes including Active Galactic Nuclei (AGN), pulsars, normal galaxies, and supernova remnants (SNRs). While the counterparts of many LAT sources can

---

<sup>2</sup>W. W. Hansen Experimental Physics Laboratory, Kavli Institute for Particle Astrophysics and Cosmology, Department of Physics and SLAC National Accelerator Laboratory, Stanford University, Stanford, CA 94305, USA

<sup>53</sup>Institut für Astronomie und Astrophysik, Universität Tübingen, D 72076 Tübingen, Germany

be spatially resolved when observed at other frequencies, detection of spatial extension of these sources at GeV energies is difficult because the size of the point-spread function (PSF) of the LAT is comparable to the typical size of many of these sources.

However, a number of sources positionally coincident with LAT sources exhibit extensions at other wavelengths which are comparable to or larger than the LAT PSF. In particular, certain SNRs, pulsar wind nebulae (PWNe), molecular clouds, normal galaxies, galaxy clusters or dark matter satellites could be expected to be detected as spatially extended sources by the LAT. The LAT Collaboration has previously reported on five SNRs which are spatially extended beyond the LAT PSF at GeV energies (IC443, W28, W44, W51C, and RX J1713.7-3946 (Abdo et al. 2010g,e,f, 2009b, 2011c)). In addition, three extended PWNe were detected: MSH 15-52, Vela X, and HESS J1825-137 (Abdo et al. 2010a; The Fermi LAT Collaboration & Timing Consortium 2010; Grondin et al. 2011), as well as two close-by galaxies, the Large and Small Magalenic Cloud (Abdo et al. 2010h,b), and finally the radio galaxy Centarus A (Abdo et al. 2010c). For each of these sources, the extension was determined from a dedicated analysis of the particular source and so a systematic scan of all LAT detected sources could uncover additional spatially extended sources.

Many extended sources in the Galactic plane have been detected at TeV energies using air Cherenkov detectors. Most prominent was a survey of the Galactic plane using the High Energy Stereoscopic System (H.E.S.S) which reported 14 spatially extended sources with extensions varying from  $\sim 0^\circ.1$  to  $\sim 0^\circ.25$  (Aharonian et al. 2006). In fact, within our Galaxy only very few sources (most notably the  $\gamma$ -ray binaries LS 5039 (Aharonian et al. 2006a), LS I+61-303 (Albert et al. 2006; Acciari et al. 2011) HESS J0632+057 (Aharonian et al. 2007c), and the Crab nebula (Weekes et al. 1989)) have no significant extension detected at TeV energies. High energy  $\gamma$ -rays from these sources are produced by the decay of  $\pi^0$ s produced by hadronic interactions with interstellar matter and by relativistic electrons due to Inverse Compton (IC) scattering and Bremsstrahlung radiation (Blandford & Eichler 1987). It is likely that the GeV and TeV emission from these sources originates from the same population of high-energy particles and so at least some of these sources should be detected as extended sources at GeV energies. By studying the spectra of these TeV sources at GeV energies, we may help to determine the emission mechanisms of these high energy sources.

The capability to spatially resolve GeV  $\gamma$ -ray sources is important for several reasons. First, multiple potential counterparts detected at other frequencies exist within the localization confidence region of a typical LAT source along the Galactic plane. Finding a coherent source extension across different energy bands can help to associate a LAT source to an otherwise confused counterpart. Also, due to the strong energy dependence of the LAT PSF, the spatial and spectral information about a source do not simply decouple. An inaccurate

spatial model will bias the spectral model of the source. Specifically, modeling a spatially extended source as point-like will systematically shift a spectral analysis to softer indices. Furthermore, correctly modeling a source’s extension is important for improving the model of the sky and removing excess residuals, for example in the region around surrounding the Large Magellanic Clouds (Abdo et al. 2010d). Such excess residuals potentially bias the significance and measured spectrum of neighboring sources in the densely populated Galactic plane.

## 2. Analysis Methods

Morphological studies of sources using the LAT are challenging because of the strongly energy-dependent PSF that is comparable in size to the extension of many sources expected to be detected at GeV energies. Additional complications arise for sources along the Galactic plane due to systematic uncertainties in the Galactic diffuse emission. The LAT’s PSF is limited at its lowest detectable energies by multiple scattering in the silicon strip tracking section of the detector and is several degrees at 100 MeV. The PSF improves with energy approaching a 68% containment radius of  $\sim 0^\circ.2$  at the highest energies (when averaged over the acceptance of the LAT) and is limited by the granularity of the silicon strips in the tracker (Atwood et al. 2009; Abdo et al. 2009e, 2011a).<sup>1</sup> However, since most high energy astrophysical sources have spectra that decrease rapidly with increasing energy, the improved resolution of the higher energy photons is offset by their low statistics. Therefore sophisticated analysis techniques are required to maximize our sensitivity to these extended sources.

### 2.1. The pointlike Package

A new analysis tool has been developed to address the unique requirements for studying spatially extended sources with the LAT. The tool performs a maximum likelihood analysis in which the Poisson likelihood for observing the measured counts is maximized, given a parametrized spatial and spectral model of the source and its surrounding region. The extension of a source can be modeled by a geometric shape (e.g. a disk or Gaussian) and the source’s position, extension, and spectrum can be simultaneously fit.

---

<sup>1</sup>More information about the performance of the LAT can be found at the Fermi Science Support Center (FSSC, <http://fermi.gsfc.nasa.gov>).

This type of analysis is not feasible using the standard LAT likelihood analysis tool `gtlike`<sup>2</sup> because `gtlike` can only fit the spectral parameters of the model unless a more sophisticated iterative procedure is used to also test various source morphologies. We note that `gtlike` has been used in the past in several studies of source extension in the LAT Collaboration (Abdo et al. 2010h,b,e, 2009b). Based upon a set of `gtlike` maximum likelihood fits at fixed extensions, a profile of the likelihood as a function of the extension was calculated. This approach is not optimal because the position, extension, and spectrum of the source must be simultaneously fit to find the best fit parameters and to correctly compute the statistical significance of the detection. Furthermore since the `gtlike` likelihood profile approach is computationally intensive, no large-scale Monte Carlo effort has been run to validate it.

The approach presented here is based on a second maximum likelihood fitting package developed in the LAT Collaboration called `pointlike` (Abdo et al. 2010d; Kerr 2011). We extended the code to allow a simultaneous fit of the source extension together with the position and the spectral parameters.

The choice to base the spatial extension fitting on `pointlike` rather than `gtlike` was made on considerations of computing time. The `pointlike` algorithm was optimized for speed to handle larger numbers of sources efficiently which is important for our catalog scan as well as the Monte Carlo validation of our method. Details on the `pointlike` package can be found in Kerr (2011).

## 2.2. Extension Fitting

In `pointlike`, it is assumed that the spatial and spectral model of an extended source are separable, i.e. that the source model  $M(l, b, E) = S(l, b) \times X(E)$  where  $S(l, b)$  is the spatial distribution and  $X(E)$  is the spectral distribution. To fit an extended source, `pointlike` convolves the extended source shape with the PSF (as a function of energy) and uses the `minuit` library to maximize the likelihood by simultaneously varying the position and extension of the source (James & Roos 1975). As will be described in Section 3, simultaneously fitting the position and extension is important to correctly calculate the statistical significance of the detection of extension. For each position and extension, the spectral parameters of the sky model are refit. To avoid projection effects, the fitted source position parameters are not the source’s longitude and latitude but instead the source’s displacement in a rotated reference frame.

---

<sup>2</sup>`gtlike` is distributed publicly by the FSSC.

The significance of the extension of a source can be calculated from  $\text{TS}_{\text{ext}}$ , which is the test statistic of the likelihood ratio test of a model with a spatially extended source and a model with a point-like source and is defined as

$$\text{TS}_{\text{ext}} = 2 \log(L_{\text{ext}}/L_{\text{ps}}) = 2(LL_{\text{ext}} - LL_{\text{ps}}) \quad (1)$$

where  $LL$  is the log of the Poisson likelihood. `pointlike` calculates  $\text{TS}_{\text{ext}}$  by fitting a source first with a spatially extended model and then as a point source. The interpretation of  $\text{TS}_{\text{ext}}$  in terms of a statistical significance is discussed in Section 3.

For extended sources with an assumed radially symmetric shape, we use a semi-analytic calculation to speed up the calculation of the expected photon distribution. The expected photon distribution can be written as

$$\text{PDF}(\vec{r}) = \int \text{PSF}(|\vec{r} - \vec{r}'|) I_{\text{src}}(\vec{r}') r' dr' d\phi' \quad (2)$$

For the LAT, the PSF can be parameterized by a *King function*

$$\text{PSF}(r) = \frac{1}{2\pi\sigma^2} \left(1 - \frac{1}{\gamma}\right) \left(1 + \frac{u}{\gamma}\right)^{-\gamma}, \quad (3)$$

where  $u = (r/\sigma)^2/2$  and  $\sigma$  and  $\gamma$  are free parameters (Kerr 2011). For radially symmetric extended sources, the angular part of the integral can be evaluated analytically

$$\begin{aligned} \text{PDF}(u) &= \int_0^\infty r' dr' I_{\text{src}}(v) \int_0^{2\pi} d\phi' \text{PSF}(\sqrt{2\sigma^2(u+v-2\sqrt{uv}\cos(\phi-\phi'))}) \\ &= \int_0^\infty dv I_{\text{src}}(v) \left(\frac{\gamma-1}{\gamma}\right) \left(\frac{\gamma}{\gamma+u+v}\right)^\gamma \times {}_2F_1\left(\gamma/2, \frac{1+\gamma}{2}, 1, \frac{4uv}{(\gamma+u+v)^2}\right). \end{aligned} \quad (4)$$

where  $v = (r'/\sigma)^2/2$  and  ${}_2F_1$  is the Gaussian hypergeometric function. This convolution formula reduces the expected photon distribution to a single numerical integral.

There will always be a small numerical discrepancy between the expected photon distribution derived from a true point source and a very small extended source due to numerical error in the convolution. In most situations, this error is insignificant. But in particular for very bright sources, this numerical error has the potential to bias the test statistic for the extension test. Therefore, when calculating  $\text{TS}_{\text{ext}}$ , we compare the likelihood fitting the source with an extended spatial model to the likelihood when fixing its extension to  $10^{-10}$  deg.

We estimate the error on the extension of a source by fixing the position of the source and varying the extension until the likelihood has fallen by  $\frac{1}{2}$ , corresponding to a  $1\sigma$  error. This method is shown schematically in Figure 1(a) which shows the change in  $LL$  when varying the extension of the SNR IC443. The localization error is calculated by fixing the extension and spectrum of the source and fitting to the likelihood function a Gaussian as a function of position.

### 2.3. `gtlike` Analysis Validation

`pointlike` is important for LAT analyses that require many iterations such as source localization and extension fitting. On the other hand, because of the fewer approximations used in calculating the likelihood we expect the spectral parameters found with `gtlike` to be slightly more precise. Furthermore, because `gtlike` is the standard likelihood analysis package, it has been more extensively validated for spectral analysis. For those reasons, in the following analysis we use `pointlike` to determinate the position and extension of a source and subsequently determine the spectrum using `gtlike`. Both `gtlike` and `pointlike` can be used to estimate the statistical significance of the extension of a source and we require that both methods agree to claim a detection.

We found good agreement between the two methods. Unless explicitly mentioned, all TS,  $TS_{\text{ext}}$ , and spectral parameters were calculated using `gtlike` using the best-fit positions and extensions found with `pointlike`.

### 2.4. Dual Localization

There is a degeneracy between a spatially extended source and multiple point sources that are separated by angular distances comparable or smaller than the size of the LAT PSF. To assess the possibility of source confusion, we developed a function in `pointlike` to simultaneously fit the position of two point sources.

We define  $TS_{\text{inc}}$  as twice the increase in  $LL$  fitting the region as two point sources compared to fitting the region as one point source:

$$TS_{\text{inc}} = 2 \times (LL_{2\text{pts}} - LL_{\text{ps}}). \quad (6)$$

$TS_{\text{inc}}$  can not be directly compared to  $TS_{\text{ext}}$  to see which model is more significant because the models are not nested (Protassov et al. 2002). Even though the comparison of  $TS_{\text{ext}}$  with  $TS_{\text{inc}}$  is not a calibrated test, we find the cases  $TS_{\text{inc}} \ll TS_{\text{ext}}$  or  $TS_{\text{inc}} \gg TS_{\text{ext}}$  suggestive and we only consider a source to be extended if  $TS_{\text{ext}} > TS_{\text{inc}}$ . Similar to the case of extended sources described in Section 2.3, the spectrum of the two point sources can be refit using `gtlike`. We quote the spectral values obtained from `gtlike` using the best fit positions found using `pointlike`.

## 2.5. Comparing Source Sizes

We tested two different models for the surface brightness profile, either a two dimensional Gaussian

$$I(x, y) = \frac{1}{2\pi\sigma^2} \exp(-(x^2 + y^2)/2\sigma^2) \quad (7)$$

or a uniform disk

$$I(x, y) = \begin{cases} \frac{1}{\pi\sigma^2} & x^2 + y^2 \leq \sigma^2 \\ 0 & x^2 + y^2 > \sigma^2 \end{cases} \quad (8)$$

Although these shapes are significantly different, their convolution with the PSF look similar. Figure 2 demonstrates this by showing  $I_{\text{src}}$ , the PSF, and the PDF for a radially symmetric uniform brightness and the Gaussian surface brightness of size 0.5.<sup>3</sup> This plot shows that the LAT is not very sensitive to probing the exact structure of an extended source. In the search for extended sources, we therefore use only a uniform disk as our spatial extension shape. We then quote the radius of the disk edge as the size of the source.

## 3. Validation of Analysis Method

We test the performance of `pointlike` fitting the extension of point-like sources. Mattox et al. (1996) discuss that the test statistic distribution for a likelihood ratio test on the existence of a source at a given position is

$$P(\text{TS}) = \frac{1}{2}(\chi_1^2(\text{TS}) + \delta(\text{TS})). \quad (9)$$

The particular form of Equation 9 is due to the null hypothesis (source flux  $\Phi = 0$ ) residing on the edge of parameter space and the model hypothesis adding a single degree of freedom. It is plausible to expect a similar distribution of the test statistic in the test for source extension as the same conditions apply (with the source flux  $\Phi$  replaced by the source radius  $r$  and  $r < 0$  being unphysical). To validate this claim, we performed a Monte Carlo study to calculate empirical distributions for  $\text{TS}_{\text{ext}}$  and compared them to Equation 9.

We simulated point sources with various spectral forms using `gtobssim`<sup>4</sup> and fit them with `pointlike` using both point and extended source hypotheses. The point sources were

---

<sup>3</sup>To allow a valid comparison between Gaussian and disk shaped morphologies, we define the source size for this test as the radius containing 68% of the intensity ( $r_{68}$ ).  $r_{68, \text{Gaussian}} = 1.51\sigma$  and  $r_{68, \text{disk}} = 0.82\sigma$  where  $\sigma$  is defined in Equation 7 and Equation 8 respectively.

<sup>4</sup>`gtobssim` is distributed publicly by the FSSC.



simulated with a power-law spectral model with integrated fluxes above 100 MeV ranging from  $3 \times 10^{-9}$  to  $10^{-6}$   $\text{ph cm}^{-2}\text{s}^{-1}$  in six discrete steps and spectral indices ranging from 1.5 to 3 in four discrete steps. These values were picked to represent typical source parameter of LAT-detected sources. The point sources were simulated on top of an isotropic background with an integrated flux above 100 MeV of  $1.5 \times 10^{-5}$  taken to be the same as the isotropic spectrum measured by EGRET (Sreekumar et al. 1998). The Monte Carlo simulation was performed over a one year observation period using a default rocking profile and a representative livetime fraction of 0.8. The reconstruction was performed using 1-100 GeV photons and the Pass 7\_V6 (P7\_V6) Source Instrument Response Function (IRFs, Abdo et al. (2011a)). For each significantly detected point source ( $\text{TS} > 25$ ), we used `pointlike` to fit it as an extended source and calculate  $\text{TS}_{\text{ext}}$ .

For each set of spectral parameters,  $\sim 30,000$  statistically independent simulations were performed. For the dimmer spectral models, many of the simulations left the source undetected ( $\text{TS} < 25$ ) and were discarded. Table 1 shows the different spectral models used in our study as well as the number of simulations. The cumulative density of  $\text{TS}_{\text{ext}}$  is plotted in Figure 3. The  $\chi^2_1/2$  distribution of Equation 9 is overlaid for comparison.

Our Monte Carlo study shows broad agreement between simulations and Equation 9. Nevertheless, the agreement is not perfect. It should be noted that the discrepancy seems to be worst for bright sources, a likely cause being numerical errors in the convolution becoming more apparent for sufficiently bright sources. Other possible reasons for departure from Equation 9 could be that `pointlike` ignores energy dispersion which would change the PSF shape as a function of energy. We emphasize that many of the empirical distributions lies to the left of the theoretical curve so using the theoretical distribution would lead to an underestimate of the statistical significance of a detection. Therefore, we are confident that  $\sqrt{\text{TS}_{\text{ext}}}$  can be used as a conservative measure of the statistical significance of a source’s extension and use it in the following analysis.

#### 4. Extended Source Detection Threshold

We calculated the LAT’s detection threshold to resolve spatially extended sources as being extended. We define the detection threshold as the flux at which the value of  $\text{TS}_{\text{ext}}$  averaged over many statistical realizations of a source is  $\langle \text{TS}_{\text{ext}} \rangle = 16$ , corresponding to a  $4\sigma$  detection (see section 3).

We used the simulation setup described in Section 3, but instead simulated extended sources with a radially symmetric uniform surface brightness and simulated over the actual



two year time interval of LAT observations. For each extension and spectral index, we selected a flux range which bracketed  $\text{TS}_{\text{ext}} = 16$  and performed an extension test for  $> 100$  independent realizations of ten flux values in this range. We calculated  $\langle \text{TS}_{\text{ext}} \rangle = 16$  by fitting a line to the flux and  $\text{TS}_{\text{ext}}$  values in this narrow range.

Figure 4 shows the threshold for sources of four spectral indices from 1.5 to 3 and extension varying from  $\sigma = 0.1$  to  $2.0$ . The LAT’s flux threshold for a significant detection of source extension drops quickly with increasing source size and reaches a minimum around  $0.5$ . Figure 4 shows the threshold using photons with energies between 100 MeV and 100 GeV and also using only 1-100GeV photons. Except for very large ( $> 1$  deg) sources, our detection threshold is not substantially improved including photons with energies between 100 MeV and 1 GeV. This is also demonstrated in Figure 1(b) which shows  $\text{TS}_{\text{ext}}$  for the SNR IC443 computed independently in twelve energy bins between 100 MeV and 100 GeV. For IC443, which has a spectral index  $\sim 2.4$ , almost the entire increase in TS comes from energies above 1 GeV. On the other hand, other systematic errors become increasingly important at low energy. For our extension search, we therefore use only photons with energies above 1 GeV.

Figure 5 shows the flux threshold as a function of source extension for different background levels (1x, 10x, and 100x the nominal background), different spectral indices, and two different energy bands (1-100 GeV and 10-100 GeV). The detection threshold is higher for sources in regions of higher background. For a fixed 1-100 GeV or 10-100 GeV flux, the LAT’s detection threshold is only weakly depends upon the spectral index. This effect is most pronounced when using only photons with energies above 10 GeV. Overlaid on Figure 5 are the LAT detected extended sources that will be discussed in Sections 6 and 8. The extension thresholds are tabulated in Table 2.

Finally, Figure 6 shows the LAT’s projected detection threshold to extension after 10 years against 10 times the isotropic background. This background is representative of the background near the Galactic plane. For small extended sources, our detection threshold improves by a factor larger than the square root of time because at high energies, where we are most sensitive to extension, the background levels are in the Poisson instead of Gaussian regime. For large extended sources, the relevant background is larger and the improvement is closer to the expected factor of the square root of time.

## 5. Extended Source Search Method

We test all sources in the second *Fermi*-LAT Catalog (2FGL) for spatial extendedness. 2FGL is a catalog of 1873 sources detected by the LAT. It included twelve previously published spatially extended sources but did not attempt to fit the extension of these sources. Other than these sources, all 2FGL sources were modeled as point sources and 2FGL did not attempt to resolve the extension of new sources.

Our analysis setup is closely related to the setup used for the derivation of the catalog. We used the same two years of data from 2008 August 4 to 2010 August 1 and we used the same Pass 7\_V6 (P7\_V6) Source class event selection and IRFs (Abdo et al. 2011a). We used the same models to describe the background from Galactic diffuse, isotropic, and earth limb emission. The galactic diffuse emission was scaled by a power-law and the isotropic component’s normalization was left free.

As was shown in Section 4, we gain little in sensitivity using photons with energies below 1 GeV. On the other hand, the large PSF at low energy makes us more susceptible to systematic errors arising from source confusion due to multiple point sources and susceptible to incorrect modeling of the Galactic diffuse emission. In addition, the Galactic diffuse emission is more pronounced at lower energies due to its steep energy spectrum. For that reason, we performed our search using photons only between 1 GeV and 100 GeV.

We also performed a search for extended sources using only 10-100 GeV photons. Even though we are testing the same sources, this approach is complimentary because the Galactic diffuse emission is even less dominant above 10 GeV. Furthermore, source confusion becomes less of a problem since most LAT sources are not significantly detected at energies exclusively above 10 GeV. So we expect to be able to resolve harder sources in more complicated regions. The  $> 10$  GeV analysis is especially beneficial for regions near pulsars which are not significantly above 10 GeV and was successfully used in detecting HESS J1825-137 and MSH 15-52 with the LAT (Abdo et al. 2010a; Grondin et al. 2011).

We tested each source for extension using `pointlike` assuming the source had a uniform radially symmetric surface brightness and a power-law spectral model. We used a circular 10 deg region of interest centered on our source and included all catalog sources within 15 deg of the source of interest in our background model. We refit the spectral parameters of sources within 2 deg of the source to avoid potential biases of the extension parameters of the source of interest due to close-by background sources.

Finally, when analyzing the region, we automatically removed other 2FGL sources which were within  $0.5^\circ$  of the source of interest. This was done to avoid a concern that extended sources are included in 2FGL as multiple point sources. These spurious sources could distort

the extension fit. Instead, when a source is found to be significantly extended (i.e.  $\text{TS}_{\text{ext}} > 16$ ), we perform the dual localization procedure (described in Section 2.4 to compare the extended source hypothesis to the hypothesis of two independent point sources. Only sources with  $\text{TS}_{\text{ext}} > \text{TS}_{\text{inc}}$  are considered as extended.

### 5.1. Additional Analysis

Based on size vs. physical distance considerations, we expect most extended sources to be located inside our Galaxy and thus to be concentrated along the Galactic plane. Unfortunately, the GeV emission in the Galactic plane is dominated by extremely structured diffuse emission from the interactions of cosmic rays with the interstellar medium. Finding sources on top of this emission is difficult (Abdo et al. 2009a) as has been discussed in 1FGL and 2FGL (Abdo et al. 2010d, 2011b). Furthermore, the Galactic plane is crowded and it is often difficult to correctly model nearby sources. Because of this, finding a source with  $\text{TS}_{\text{ext}} > 16$  is not a sufficient criteria for resolving a source. For each extended source, we perform several analysis crosschecks.

For each candidate, we generated a map of residual TS by adding a new source of spectral index 2 into the region and finding the increase in likelihood when fitting its flux. TS maps are useful to look for residual structure in the sky model. Figure 7 shows a residual TS map for the extended source IC443. The residual TS map indicates that the spatially extended model for IC443 is a significantly better description of the observed photons. We also generated plots of the sum of all counts within a given distance of the source and compared it to the model predictions of a point source. An example radial integral plot is shown for the extended source IC443 in Figure 1(c). For each source, we also made diffuse-emission-subtracted smoothed counts maps. Figure 1(d) shows an example for IC443.

We then inspected the residual TS, smoothed counts maps, and radial integral distributions to identify cases in which the extension fit is clearly influenced by large-scale residuals in the diffuse emission and hence the extension measurement unreliable. An example of such a case is shown in Figure 8. It shows a Galactic and isotropic diffuse-emission-subtracted smoothed counts map of this source using 1-100 GeV photons. In this region along the Galactic plane, there appears to be large-scale residual in the diffuse emission. As a result, 2FGL J1856.2+0450c fit to an extension of  $1.83^\circ$  and the result is statistically significant with  $\text{TS}_{\text{ext}} = 45.4$ . However, by looking at the residuals it is clear that this complicated region is not fit well even though the source’s extension is statistically significant. We do not report sources as extended that fail this inspection.

For the remaining candidates, we took the spatial and spectral model found using `pointlike` and re-determined the spectral parameters using `gtlike`. We used the ‘binned likelihood’ mode of `gtlike` on a  $14\text{ deg} \times 14\text{ deg}$  ROI with a pixel size of  $0.03$ . We obtained a second measure of  $\text{TS}_{\text{ext}}$  from `gtlike` for the extension and position of the source as determined by `pointlike`. We only considered a source to be significantly extended if  $\text{TS}_{\text{ext}} > 16$  with both `pointlike` and `gtlike`.

Because of the high source density in the Galactic plane, for promising candidates we often had to iteratively improve the model of our background sources to obtain a better fit of the sources. Several catalog sources would often fill in the emission of the extended source and would have to be removed from the region. Similarly, background sources were often insignificant in the fit energy range and had to be removed. The position of background sources would often have to be refit once the extended source was fit. When the model of the extended source coupled strongly with nearby sources, we iteratively fit the extended source and all nearby sources until the fit converged. For each extended source, we describe the modifications of the background model compared to the model used in the creation of the 2FGL catalog that were required.

## 5.2. Systematic Errors on Extension

We estimate a systematic error on the extension of a source due to uncertainty in our knowledge of the LAT PSF. Before launch, the LAT PSF was determined by a detector simulation which was verified in accelerator tests (Atwood et al. 2009). However, in-flight data revealed a discrepancy above a few GeV in the PSF compared to the photon angular distribution of bright AGN. A publication on this issue is in preparation (Abdo et al. 2011a). Subsequently, the PSF was fit empirically to bright AGN and this empirical parameterization is the default PSF used in the P7\_V6 IRFs. To account for this uncertainty in our knowledge of the PSF, we refit our extended source candidates using the Monte Carlo representation of the PSF and consider the difference in extension found using the two PSFs as a systematic error on the extension of a source. The same approach was used in (Abdo et al. 2010g). At high energies, we believe that our parameterization of the PSF from bright AGN is substantially better than the Monte Carlo representation of the PSF so this estimate of systematic errors is conservative.

We estimate a second systematic error on the extension of a source due to uncertainty in the model of the Galactic diffuse emission by using an alternative diffuse model. An al-

ternative model was based upon GALPROP<sup>5</sup> and used in the LAT analysis of the isotropic diffuse emission (Abdo et al. 2010i). The intensities of various components to the galactic diffuse emission are then fitted individually using a spatial distribution of the intensities within the ROI as predicted by the model. We distinguish contributions from CR interactions with the molecular hydrogen, the atomic+ionized hydrogen, residual gas traced by dust (Grenier et al. 2005), and the interstellar radiation field. We further split the contributions from interactions with molecular and atomic hydrogen to the Galactic diffuse emission according to the distance from the Galactic center in which they are produced. Hence, we replace the standard diffuse emission model by 18 individually fitted templates to describe individual components of the diffuse emission. A similar crosscheck was used in the LAT Collaboration’s analysis of RX J1713.7-3946 (Abdo et al. 2011c).

It is not expected that this diffuse model is superior to the standard LAT model that was obtained through an all-sky fit. But adding degrees of freedom to the background model can remove likely spurious sources that correlate with features in the Galactic diffuse emission. Therefore, this tests systematics that may be due to incorrect modeling of the diffuse emission in the region.

We do not except the systematic error due to uncertainties in the PSF to be correlated to the systematic due to uncertainty in the Galactic diffuse emission so the total systematic error on the extension of a source so we obtain the total systematic error by adding them in quadrature.

## 6. Analysis of Extended Sources Identified in 2FGL

We first present on our analysis of the twelve extended sources included in 2FGL. (Abdo et al. 2011b). The six extended SNRs IC443, W28, W30, W44, W51C, and the Cygnus Loop were included in 2FGL. IC443, W28, W44, W51C, and the Cygnus Loop were first reported in Abdo et al. (2010g,e,f, 2009b); Katagiri et al. (2011). A detailed publication by the LAT Collaboration about W30 is still in preparation. GeV emission from W30 was also studied in Castro & Slane (2010). Using 1-100 GeV photons, our analysis significantly detected the extension of all six SNRs.

Two nearby satellite galaxies of the Milky Way the Large Magalenic Cloud (LMC) and the Small Magalenic Cloud (SMC) were included in 2FGL as spatially extended sources

---

<sup>5</sup>GALPROP is a software package for calculating the Galactic  $\gamma$ -ray emission based on a model of cosmic-ray propagation in the Galaxy. See <http://galprop.stanford.edu/> for details and references

(Abdo et al. 2010h,b). They were significantly detected using 1-100 GeV photons. Our fit extension is comparable to the published result, but we note that previous LAT Collaboration publication on LMC used a more complicated two Gaussian surface brightness spatial model when fitting it ((Abdo et al. 2010h)).

Three PWNe Vela X, MSH 15-52, and HESS J1825-137 were already identified in 2FGL (The Fermi LAT Collaboration & Timing Consortium 2010; Abdo et al. 2010a; Grondin et al. 2011). HESS J1825-137 was significantly detected using 10-100 GeV photons. To improve the model of this source, we removed the nearby catalog source 2FGL J1823.1-1338c which is part of the extended source. To avoid confusion with the nearby bright pulsar PSR J1509-5850, MSH 15-52 must be analyzed at high energies. Using photons with energies above 10 GeV, we fit the extension of MSH 15-52 to be consistent with the published size with an extension significance of  $TS_{\text{ext}}=6.5$ .

Our analysis was unable to resolve Vela X which would have required first removing the pulsed photons from the Vela pulsar which is beyond the scope of this paper. Our analysis also failed to detect a significant extension for the Centaurus A Lobes (Abdo et al. 2010c). This is because the source’s emission is significantly different from a uniform radially symmetric surface brightness.

Our analysis of these sources is summarized in Table 3. This table includes the best fit position and extension of these sources when fitting them as disk-shaped sources with a radially symmetric uniform surface brightness. It also includes the best fit spectral parameters for each source. The position and extension of Vela X and the Centaurus A Lobes are included in this list for completeness.

## 7. Test of 2LAC Sources

To validate our method, we test LAT sources associated with AGN for extension. GeV emission from AGN is believed to originate from the cores of kpc-scale jets of distant galaxies. Therefore AGN are not expected to be spatially resolvable by the LAT and provide a good calibration source to demonstrate the efficacy of our tool. We note that mpc-scale  $\gamma$ -ray halos around AGNs have been hypothesized (Aharonian et al. 1994) which could be resolved by the LAT. However, no such halo has been discovered in the LAT data so far.

Following 1FGL, the LAT Collaboration published a list of sources that had a high probability association with AGN called 1LAC (Abdo et al. 2010j). 1FGL had 709 1FGL sources associated with 671 distinct AGN at high latitude ( $|b| > 10^\circ$ ). Using two years of data and 2FGL, the LAT Collaboration associated 1016 2FGL sources with AGN called

2LAC (Ackermann et al. 2011). To avoid systematic problems with AGN classification, we selected 885 out of the 1016 AGN which made it into the clean AGN sub-sample. An AGN association is considered clean only if it has a high probability of association  $P \geq 80\%$ , if it is the only AGN associated with the catalog source, and if there are no flags on the source in 2FGL. These last two conditions are important for our analysis. Source confusion may look like a spatially extended source and flagged catalog sources may correlate with unmodeled structure in the diffuse emission.

Of the 885 clean AGN, we select 783 of these 2FGL sources which are significantly detected above 1 GeV and fit each of them for extension. A histogram of the  $\text{TS}_{\text{ext}}$  values computed for these AGN is shown in Figure 9. Overlaid on the plot is the  $\chi^2/2$  distribution of Equation 9. The  $\text{TS}_{\text{ext}}$  distribution for AGN shows good agreement with the theoretical distribution. Two sources had  $\text{TS}_{\text{ext}} > 10$ . One was due to incorrectly automatically removing a nearby catalog sources (see Section 5) and the other was due to a failure of convergence of the point hypothesis. This result demonstrates that we can use  $\text{TS}_{\text{ext}}$  as a measure of the statistical significance of the detection of the extension of a source.

We should clarify that the LAT PSF used in this study was determined empirically by fitting the observed shape of bright AGN (see Section 5.2). Finding that the AGN we test are not extended is not surprising. This validation analysis is not suitable to reject any hypotheses about the existence of mpc-scale halos around AGN.

## 8. New Extended Sources

Nine extended sources not included in 2FGL were found using this search. Three were found in our search using 1-100 GeV photons and six were found in our search using 10-100 GeV photons. The fit properties of these nine sources is summarized in Table 4. This table includes for each source the best fit position, extension, spectrum, source significance, and significance of extension.

The results of our investigation of systematic uncertainties of this measurement are presented in Table 5. It shows a comparison between the fit with a single extended source hypothesis and the fit assuming the emission originates from two independent sources and the results of the extension fit using variations of the PSF and the galactic diffuse model described in Section 5.2. There is good agreement between  $\text{TS}_{\text{ext}}$  and the fit size using the standard analysis, the alternative diffuse models, and the alternative PSF. This suggests that the sources are robust against features in the diffuse model and uncertainties in the angular resolution.



### 8.1. 2FGL J0823.0-4246

The source 2FGL J0823.0-4246 was found using 1-100 GeV photons to have an extension of  $0.37 \pm 0.03_{\text{stat}} \pm 0.02_{\text{sys}}$  with an extension significance of  $\text{TS}_{\text{ext}} = 46.3$ . The source was fit to a position of  $(l, b) = (260.32, -3.28)$ . This source is coincident with the one year catalog source 1FGL J0823.3-4248. Figure 10 shows a counts map of this source and Figure 18(a) shows the LAT spectrum of it.

To get a good fit of the source, we had to remove the nearby catalog sources 2FGL J0823.4-4305 and 2FGL J0821.0-4254 which are part of the extended source. We tested the source for source confusion by fitting it as two point sources. Because  $\text{TS}_{\text{inc}} = 22.1$  is smaller than  $\text{TS}_{\text{ext}}$ , we conclude that this is an extended source. These modifications are shown in Figure 10.

1 This extended source is spatially coincident with the middle-aged SNR Puppis A. Puppis A has been studied in detail in radio (Castelletti et al. (2006), and references therein) and X-ray (Petre et al. (1996); Hwang et al. (2008), and references therein) Mosaic *ROSAT* observations of Puppis A produced the highest resolution X-ray image of the source and contours corresponding to this image are overlaid on Figure 10 and match the inferred GeV size (Petre et al. 1996). Puppis A’s distance was estimated at 2.2 kpc (Reynoso et al. 1995, 2003) which leads to a 1-100 GeV luminosity of  $\sim 3 \times 10^{34}$  ergs/s.

No molecular clouds have been observed directly adjacent to Puppis A (Paron et al. 2008). This is similar to the LAT detected SNR the Cyngus Loop (Katagiri et al. 2011). The luminosity of Puppis A is also smaller than that of other SNRs believed to interact with molecular clouds (Abdo et al. 2009b, 2010g,f,e; The Fermi-LAT Collaboration 2010). The GeV emission could therefore be explained by the interaction of accelerated particles by interstellar matter or fields, similar to the emission mechanism suggested for the Cygnus Loop SNR (Katagiri et al. 2011).

### 8.2. 2FGL J1627.0-2425c

The source 2FGL J1627.0-2425c was found using 1-100 GeV photons to have an extension of  $0.41 \pm 0.05_{\text{stat}} \pm 0.02_{\text{sys}}$  with an extension significance of  $\text{TS}_{\text{ext}} = 31.1$ . The best fit position is  $(l, b) = (353.08, 16.78)$ . This source is coincident with the one year catalog source 1FGL J1628.6-2419c. A counts map showing this source is seen in Figure 11. To test for source confusion, we also fit the source instead as two point sources. Since  $\text{TS}_{\text{inc}} = 20.0$  is smaller than  $\text{TS}_{\text{ext}}$ , we conclude that this is an extended source.

This source is in a region of remarkably complicated diffuse emission. Even though it is 16 deg from the Galactic plane, the source is on top of the core of the Ophiuchus molecular cloud which contains massive star-forming regions that are bright in the infrared. The region also has abundant molecular and atomic gas traced by CO and HI but also plenty of dark gas, the kind that we find only by its association with dust emission (Grenier et al. 2005). Embedded star-forming regions make it even more challenging to measure the column density of dust. Infrared and  $^{12}\text{CO}$  ( $J = 1 \rightarrow 0$ ) contours are overlaid on Figure 11. There is good spatial correlation with the GeV emission (Young et al. 1986; de Geus et al. 1990) so this source might represent an inadequacy in the diffuse  $\gamma$ -ray model.

### 8.3. 2FGL J1712.4-3941

The source 2FGL J1712.4-3941 was found using 1-100 GeV photons to have an extension  $0^\circ56 \pm 0^\circ04_{\text{stat}} \pm 0^\circ02_{\text{sys}}$  with an extension significance of  $\text{TS}_{\text{ext}} = 39.6$ . This source was fit to a position of  $(l, b) = (347^\circ25, -0^\circ54)$ . The source is coincident with the one year catalog source 1FGL J1711.7-3944c. Figure 12 shows a smoothed counts map of this source.

This source is spatially coincident with the SNR RX J1713.7-3946 and was recently reported by (Abdo et al. 2011c). Figure 12 overlays H.E.S.S. TeV contours of SNR RX J1713.7-3946 from (Aharonian et al. 2007b). To analyze this source, we used the same background model as the recent LAT publication. 2FGL J1715.4-4024c is spatially coincident with Source A and was moved to  $(\text{RA}, \text{Dec}) = (258.84, -40.46)$ . Source B was added at  $(\text{RA}, \text{Dec}) = (258.71, -38.70)$  and Source C was added at  $(\text{RA}, \text{Dec}) = (257.47, -39.75)$ .

### 8.4. 2FGL J0851.7-4635

The source 2FGL J0851.7-4635 was found using 10-100 GeV photons to have an extension of  $1^\circ13 \pm 0^\circ08_{\text{stat}} \pm 0^\circ05_{\text{sys}}$  with an extension significance of  $\text{TS}_{\text{ext}} = 87.2$ . The source was fit to a position of  $(l, b) = (266^\circ29, -1^\circ43)$ . Figure 13 shows a counts map of this source.

2FGL J0851.7-4635 is spatially coincident with the SNR Vela Jr. Overlaid on Figure 13 are contours of Vela Jr. as seen in TeV by H.E.S.S (Aharonian et al. 2007a). The GeV and TeV morphology match well. A detailed papers by the LAT Collaboration on Vela Jr. is in preparation.

To get a good fit of the source, we had to remove thee nearby catalog sources 2FGL J0853.5-4711, 2FGL J0848.5-4535, and 2FGL J0855.4-4625 which are part of the extended source. In addition, we relocalized the position of the nearby catalog source 2FGL J0854.7-4501 to

$(l, b) = (266^\circ 24, 0^\circ 49)$  to better fit its position at high energies in the presence of the extended source. In addition, we removed the further away catalog sources 2FGL J0858.0-4815 and 2FGL J0901.7-4655 because they were not significant above 10 GeV. After modifying the region, we found that  $TS_{\text{inc}} = 16.1$  which is less than  $TS_{\text{ext}}$  so we conclude that the source is extended.

### 8.5. 2FGL J1615.0-5051

The source 2FGL J1615.0-5051 was found using 10-100 TeV photons to have an extension of  $0^\circ 33 \pm 0^\circ 04_{\text{stat}} \pm 0^\circ 01_{\text{sys}}$  with an extension significance of  $TS_{\text{ext}} = 16.3$ . The source was fit to a position of  $(l, b) = (332^\circ 38, -0^\circ 14)$ . This source is coincident with the one year catalog source 1FGL J1613.6-5100c. Figure 14 shows a counts map of this source.

This source is less than 1 deg away from 2FGL J1615.2-5138 which is also spatially extended (see Section 8.6). To get a good fit of both sources, we had to model both sources as being spatially extended and iteratively fit the position and extension of each source until obtaining a global best fit. Before doing this, We removed from our model the source 2FGL J1614.9-5212 because it is part of 2FGL J1615.2-5138's. Furthermore, we removed the nearby catalog sources 2FGL J1619.7-5040c and 2FGL J1620.6-5111c because they were not significant above 10 GeV. These modifications are further described in the caption to Figure 14. After modifying the region, we found that  $TS_{\text{inc}} = 11.9$  which is less than  $TS_{\text{ext}}$  so we conclude that the source is extended.

2FGL J1615.2-5138 is spatially coincident with the extended TeV source HESS J1616-508 (Aharonian et al. 2006). In Figure 14, contours of HESS J1616-508 are overlaid on 2FGL J1615.0-5051. The H.E.S.S. experiment measured an extension  $0.136 \pm 0.008$  when fitting the source with an elliptical Gaussian surface brightness. This size corresponds to a 68% containment radius of  $r_{68} = 0^\circ 21 \pm 0^\circ 01$ . This size is comparable to the LAT size  $r_{68} = 0^\circ 27 \pm 0^\circ 03$  (see Section 2.5). Figure 19(a) shows that the LAT spectrum of 2FGL J1615.0-5051 connects smoothly to the H.E.S.S spectrum of HESS J1616-508.

HESS J1616-508 is located in the region of two SNRs, RCW103 (G332.4-04) and Kes 32 (G332.4+0.1) but is not spatially coincident with either of them (Aharonian et al. 2006). HESS J1616-508 is near three pulsars PSR J1614-5048, PSR J1616-5109, and PSR J1617-5055 but only PSR J1617-5055 is energetically favored as being the TeV emitter (Torii et al. 1998; Landi et al. 2007a). Aharonian et al. (2006) speculated that a PWN powered by this young pulsar could be responsible for the emission of HESS J1616-508. Because HESS J1616-508 is  $9'$  away from PSR J1617-5055, this would require an assymetric X-ray PWNe to

power the TeV emission. However, *Chandra* ACIS observations revealed only an underluminous PWN of about  $\sim 1'$  size around the pulsar which was not oriented towards the TeV emission, rendering this association as uncertain (Kargaltsev et al. 2009). No other promising counterparts were observed in observations of x-ray and soft gamma-ray emission by *Suzaku* (Matsumoto et al. 2007), *Swift*/XRT, IBIS/ISGRBI, BeppoSAX and *XMM-Newton* (Landi et al. 2007a). Finally, Kargaltsev et al. (2009) found diffuse emission towards the center of HESS J1616-508 using archival radio and infrared observations. Deeper observations will likely be necessary to understand this region.

## 8.6. 2FGL J1615.2-5138

The source 2FGL J1615.2-5138 was found using 10-100 GeV photons to have an extension of  $0^\circ.42 \pm 0^\circ.03_{\text{stat}} \pm 0.01_{\text{sys}}$  with an extension significance of  $\text{TS}_{\text{ext}} = 48.0$ . The source was fit to a position of  $(l, b) = (331^\circ.66, -0^\circ.66)$ . This source is coincident with the one year catalog source 1FGL J1614.7-5138c. Because 2FGL J1615.2-5138 is close to 2FGL J1615.0-5051, the same model described in Section 8.5 was used to analyze both sources. Both sources can be seen in Figure 14. For 2FGL J1615.2-5138,  $\text{TS}_{\text{inc}} = 37.0$  which is less than  $\text{TS}_{\text{ext}}$  so we conclude that the source is extended.

This source is spatially coincident with the extended TeV source HESS J1614-518 (Aharonian et al. 2006). In Figure 14, contours of HESS J1614-518 are overlaid on 2FGL J1615.2-5138. The H.E.S.S. experiment measured a Gaussian extension of  $\sigma = 0^\circ.23 \pm 0^\circ.02$  and  $\sigma = 0.15 \pm 0.02$  in the semi-major and semi-minor axis. This size corresponds to a 68% containment size of  $r_{68} = 0^\circ.35 \pm 0^\circ.03$  and  $0.23 \pm 0.03$ . This elliptical size matches the LAT size  $r_{68} = 0^\circ.35 \pm 0^\circ.03$ . Figure 19(b) shows that the LAT spectrum of 2FGL J1615.2-5138 connects smoothly to the H.E.S.S. spectrum of HESS J1614-518. Further data collected by H.E.S.S. in 2007 helped to resolve a double peaked structure in the H.E.S.S. data but no spectral variation across the source, suggesting that the emission is not the confusion of physically separate sources (Rowell et al. 2008). The source was also detected by CANGAROO-III (Mizukami et al. 2011).

There are five nearby pulsars, but none are luminous enough to provide the required energy output required to power the TeV emission (Rowell et al. 2008). HESS J1614-518 is spatially coincident with a young open cluster Pismis 22 (Landi et al. 2007b; Rowell et al. 2008). *Suzaku* detected two promising x-ray candidates. Source A is an extended source consistent with the peak of HESS J1614-518 and source B coincident with Pismis 22 and towards the center but in a relatively dim region of HESS J1614-518 (Matsumoto et al. 2008). Three hypothesis have been presented to explain this emission; either source A is an SNR

powering the  $\gamma$ -ray emission, source A is a PWN powered by an undiscovered pulsar in either source A or B, and finally that the emission may arise from hadronic acceleration in the stellar winds of Pisim 22 (Mizukami et al. 2011).

### 8.7. 2FGL J1632.4-4753c

The source 2FGL J1632.4-4753c was found using 10-100 GeV photons to have an extension of  $0^\circ.44 \pm 0^\circ.04_{\text{stat}} \pm 0^\circ.03_{\text{sys}}$  with an extension significance of  $\text{TS}_{\text{ext}} = 64.5$ . The source was fit to a position of  $(l, b) = (336^\circ.41, 0^\circ.22)$ . This source is coincident with the one year catalog source 1FGL J1632.9-4802c. Figure 15 shows a counts map of this source.

To get a good fit of the source, we had to remove from our model three catalog sources 2FGL J1631.7-4720c, 2FGL J1630.2-4752, 2FGL J1634.4-4743c.4-4820c that were part of the extended source.. We then iteratively relocalized the source 2FGL J1635.4-4717c to  $(l, b) = (337^\circ.23, 0^\circ.35)$  and 2FGL J1636.3-4740c to  $(l, b) = (336^\circ.97, -0^\circ.07)$  while fitting the extension of 2FGL J1632.4-4753c. In addition we removed from our model four farther away two year catalog sources 2FGL J1638.0-4703c, 2FGL J1628.1-4857c, 2FGL J1630.1-4615, 2FGL J1639.8-4921c because they were not significant above 10 GeV. These modifications are shown in Figure 15. To test for source confusion, we compared the likelihood fitting this region as one extended source to the likelihood fitting this region as two point sources. We found  $\text{TS}_{\text{inc}} = 40.6$  which is less than  $\text{TS}_{\text{ext}}$  so we conclude that this is an extended source.

This extended source is spatially coincident with the extended TeV source HESS J1632-478 (Aharonian et al. 2006). In Figure 15, contours of HESS J1632-478 are overlaid on 2FGL J1635.4-4717c. H.E.S.S. measured a extension of  $\sigma = 0.21 \pm 0.05$  and  $0.06 \pm 0.04$  along the semi-major and semi-minor axes when fitting the source with an elliptical Gaussian surface brightness. This corresponds to a 68% containment size  $r_{68} = 0^\circ.31 \pm 0^\circ.08$  and  $0^\circ.09 \pm 0^\circ.06$  along the semi-major and semi-minor axis. This size is consistent with the LAT size  $r_{68} = 0^\circ.36 \pm 0^\circ.04$ . Figure 19(c) shows that the LAT spectrum of 2FGL J1635.4-4717c connects smoothly to the H.E.S.S. spectrum of HESS J1632-478.

Aharonian et al. (2006) argued that HESS J1632-478 is positionally coincident with the hard X-ray source IGR J1632-4751 observed by INTEGRAL, *XMM-Newton*, and *ASCA* (Tomsick et al. 2003; Rodriguez et al. 2003; Sugizaki et al. 2001), but this source is suspected to be an galactic X-Ray Binary so the  $\gamma$ -ray extension disfavors the association. Further observations by *XMM-Newton* reveal extended emission of size  $\sim 32'' \times 15''$  and inside point-like emission coincident with the peak H.E.S.S. emission (Balbo et al. 2010). They found in archival MGPS-2 data a spatially coincident extended radio source (Murphy et al.

2007). The positional match argues for a single synchrotron processes producing X-ray and GeV and TeV radiation, likely due to a PWNe. The increased GeV and TeV size compared to the X-ray size has previously been observed in several aging PWNe including HESS J1825-137 (Gaensler et al. 2003; Aharonian et al. 2006b), HESS J1640-465 (Aharonian et al. 2006; Funk et al. 2007), and Vela X (Markwardt & Ogelman 1995; Aharonian et al. 2006c). This can be explained by a different synchrotron cooling time for the electrons producing X-rays and TeV gamma rays.

### 8.8. 2FGL J1837.3-0700c

The source 2FGL J1837.3-0700c was found with 10-100 GeV photons to have an extension of  $0^\circ.35 \pm 0^\circ.08_{\text{stat}} \pm 0^\circ.03_{\text{sys}}$  with an extension significance of  $\text{TS}_{\text{ext}} = 18.8$ . The source was fit to a position of  $(l, b) = (25^\circ.08, 0^\circ.13)$ . This source is coincident with the one year catalog source 1FGL J1837.5-0659c. Figure 16 shows a counts map of this source.

This source is in a complicated region. There are three nearby catalog sources 2FGL J1834.7-0705c, 2FGL J1836.8-0623c, and 2FGL J1839.3-0558c. To get a good fit of 2FGL J1837.3-0700c, we relocalized 2FGL J1834.7-0705c to  $(l, b) = (24^\circ.77, 0^\circ.50)$ , 2FGL J1836.8-0623c to  $(l, b) = (25^\circ.57, 0^\circ.32)$ , and 2FGL J1839.3-0558c to  $(l, b) = (26^\circ.08, 0^\circ.23)$ . We removed the nearby catalog source 2FGL J1835.5-0649 which is part of the extended source and also the farther away catalog source 2FGL J1839.0-0539 because it was not significant above 10 GeV. These modifications are shown in Figure 16. After modifying the region, we found that  $\text{TS}_{\text{inc}} = 12.6$  which is less than  $\text{TS}_{\text{ext}}$ , so we conclude that the source is spatially extended.

This source is spatially coincident with the TeV source HESS J1837-069 (Aharonian et al. 2006). In Figure 16, contours of HESS J1837-069 are overlaid on 2FGL J1837.3-0700c. H.E.S.S. measured an extension of  $\sigma = 0.12 \pm 0.02$  and  $0.05 \pm 0.02$  along the semi-major and semi-minor axis when fitting the source with an elliptical Gaussian surface brightness. This corresponds to a 68% containment radius of  $r_{68} = 0^\circ.18 \pm 0^\circ.03$  and  $0^\circ.08 \pm 0^\circ.03$  along the semi-major and semi-minor axis. The size is comparable to LAT which fit a 68% containment radius of  $r_{68} = 0^\circ.29 \pm 0^\circ.07$ . the size difference is not significant (less than 2 sigma). Figure 19(d) shows that the LAT spectrum connects smoothly to the H.E.S.S spectrum of HESS J1837-069.

HESS J1837-069 is coincident with the hard and steady X-ray source AX J1838.0-0655 (Hertz & Grindlay 1988; Bamba et al. 2003; Malizia et al. 2005; Landi et al. 2006; Gotthelf & Halpern 2008; Anada et al. 2009). This source was discovery by RXTE to be a pulsar sufficiently luminous to power the TeV emission. AX J1838.0-0655 was spatially re-



solved by *Chandra* to be a bright point source surrounded by a  $\sim 2'$  nebula (Gotthelf & Halpern 2008) and so the  $\gamma$ -ray emission may be powered by this pulsar. A second X-ray point source AX J1837.3-0652 is in the region of HESS J1837-069 (Bamba et al. 2003; Landi et al. 2006; Gotthelf & Halpern 2008; Anada et al. 2009). It was also resolved into point-like and diffuse component although no pulsations have yet been detected from it (Gotthelf & Halpern 2008). If AX J1838.0-0655 is a pulsar/PWN powering HESS J1837-069, some of the TeV emission may also come from AX J1837.3-0652.

### 8.9. 2FGL J2021.5+4026

The source 2FGL J2021.5+4026 was found with 10-100 GeV photons to have an extension of  $0^\circ59 \pm 0^\circ03_{\text{stat}} \pm 0^\circ02_{\text{sys}}$  with an extension significance of  $\text{TS}_{\text{ext}} = 116.4$ . The source was fit to a position of  $(l, b) = (78^\circ18, 2^\circ19)$ . This source is coincident with the one year catalog source 1FGL J2020.0+4049. Figure 17 shows a counts map of this source. and Figure 18(b) shows that the LAT spectrum of it.

To get a good fit of the source, we had to remove the nearby catalog source 2FGL J2019.1+4040 which were part of the extended source. Further, we found it necessary to add an additional point source not in the two year catalog into our background model. The new source is was localized to a position of  $(l, b) = (78^\circ85, 2^\circ67)$  and had  $\text{TS} = 13.5$ . Although the source is not very significant, not including it into the background model appeared visually to significantly throw off the fit of the region. In addition, we removed the four further away catalog sources 2FGL J2022.8+3843c, 2FGL J2020.0+4159, 2FGL J2013.8+4115c, and 2FGL J2012.4+3955c from the region because they were not significant above 10 GeV. After modifying the region, we found that  $\text{TS}_{\text{inc}} = 24.3$  which is less than  $\text{TS}_{\text{ext}}$ , so we believe that this source is spatially extended. These modifications are further described in the caption to Figure 17.

This extended sources is coincident with 2CG 078+01 and 3EG J2020+4017 detected by COS B and EGRET respectively (Swanenburg et al. 1981; Hartman et al. 1999). This source is spatially coincident with the  $\gamma$ -Cygni SNR and has been speculated to be the interaction of accelerated particles in the SNR interacting with dense molecular clouds (Pollock 1985; Gaisser et al. 1998). But this association was disfavored when the LAT GeV emission from this source was detected to be pulsed (PSR J2021+4026, Abdo et al. (2010k)).

Milagro detected a  $4.2\sigma$  excess at energies  $\sim 30\text{TeV}$  from the location of this source in the previous LAT bright  $\gamma$ -ray source list. Abdo et al. (2009c,d). Veritas also detected an extended source VER J2019+407 coincident with the SNR above 200 GeV and suggested the TeV emission could be a shock-cloud interaction in  $\gamma$ -Cygni (Weinstein & for the VERITAS Collaboration



2009). Using just 10-100 GeV photons to avoid PSR J2021+4026, we resolve an extended source whose inferred GeV size well matches the radio size of  $\gamma$ -Cygni, as can be seen in Figure 17 which overlays contours of  $\gamma$ -Cygni at 408MHz from the Canadian Galactic Plane Survey (Taylor et al. 2003).

## 9. Discussion

2FGL reported on the detection of twelve sources previously known as extended. Using two years of LAT data and a new analysis method, we present on the detection of nine additional extended sources. We also reanalyze the spatial shape of the extended sources in 2FGL. Finding a coherent source extension with different frequencies, especially at TeV energies, allows us to firmly associate the LAT source in many cases.

The position of the 21 extended LAT sources are close to the Galactic plane and plotted in Figure 20. Most of the extended sources are indeed expected to be of Galactic origin as the distance of extragalactic sources (with exception of the local group Galaxies) is typically too large to resolve them in gamma rays.

Figure 23 shows a comparison of the spectral index of LAT detected extended sources and of all sources in 2FGL. This, and Table 3 and 4, show that the LAT observes a population of hard (index  $< 2$ ) extended sources above 10 GeV which connects to TeV sources. Figure 19 shows the LAT energy spectrum of four of the extended sources which were first discovered in the H.E.S.S. Galactic plane survey (Aharonian et al. 2006) and have a matching size to LAT extended sources. The LAT energy spectrum connects smoothly to TeV. This is also true of HESS J1825-137 (Grondin et al. 2011) and RX J1713.7-3946 (Abdo et al. 2011c).

For the LAT extended sources also seen in TeV, Figure 21 shows a comparison of their sizes. There is a good correlation between the GeV and TeV sizes of the sources. Even so, the size of PWNe are expected to vary across the GeV and TeV energy range and the size of HESS J1825-137 was seen by H.E.S.S. to vary between 200 GeV and 20 TeV (The H. E. S. S. Collaboration: S. Funk et al. 2007). HESS J1825-137 is significantly larger in GeV than TeV (Grondin et al. 2011). It is interesting to compare the GeV and TeV size of other PWN candidates, but definitively measuring this would require a more in-depth analysis of the LAT data using the same elliptical surface brightness model.

Figure 22 compares the size of the 21 extended LAT sources to the 42 extended H.E.S.S. sources. Because of the large field of view and all-sky coverage, the LAT can more easily measure larger sources including the LMC and SMC. On the other hand, the smaller angular resolution of Air Cherenkov detectors allows them to measure a population of extended

sources below our sensitivity limit (currently at about  $\sim 0^\circ 2$ ). *Fermi* has a five year nominal livetime with a goal of ten years of operation. As Figure 6 shows, our sensitivity to these smaller sources will improve by a factor greater than the square root of time. With increased exposure, the LAT will likely begin to resolve these smaller TeV sources.

## REFERENCES

- Abdo, A. A., et al. 2009a, Physical Review Letters, 103, 251101
- . 2009b, ApJ, 706, L1
- . 2009c, ApJS, 183, 46
- . 2009d, ApJ, 700, L127
- . 2009e, Astroparticle Physics, 32, 193
- . 2010a, ApJ, 714, 927
- . 2010b, A&A, 523, A46+
- . 2010c, Science, 328, 725
- . 2010d, ApJS, 188, 405
- . 2010e, ApJ, 718, 348
- . 2010f, Science, 327, 1103
- . 2010g, ApJ, 712, 459
- . 2010h, A&A
- . 2010i, Physical Review Letters, 104, 101101
- . 2010j, ApJ, 715, 429
- . 2010k, ApJS, 187, 460
- . 2011a, Astroparticle Physics, in preparation
- . 2011b, ArXiv e-prints
- . 2011c, ApJ, 734, 28

- 717 Acciari, V. A., et al. 2009, *ApJ*, 698, L133
- 718 —. 2011, ArXiv e-prints
- 719 Ackermann, M., et al. 2011, ArXiv e-prints
- 720 Aharonian, F., et al. 2005, *A&A*, 435, L17
- 721 —. 2006a, *A&A*, 460, 743
- 722 —. 2006b, *A&A*, 460, 365
- 723 —. 2006c, *A&A*, 448, L43
- 724 Aharonian, F., et al. 2006, *Astrophys. J.*, 636, 777
- 725 Aharonian, F., et al. 2007a, *ApJ*, 661, 236
- 726 —. 2007b, *A&A*, 464, 235
- 727 —. 2008, *A&A*, 481, 401
- 728 Aharonian, F. A., Coppi, P. S., & Voelk, H. J. 1994, *ApJ*, 423, L5
- 729 Aharonian, F. A., et al. 2007c, *A&A*, 469, L1
- 730 Albert, J., et al. 2006, *Science*, 312, 1771
- 731 Anada, T., Ebisawa, K., Dotani, T., & Bamba, A. 2009, *PASJ*, 61, 183
- 732 Atwood, W. B., et al. 2009, *ApJ*, 697, 1071
- 733 Balbo, M., Saouter, P., Walter, R., Pavan, L., Tramacere, A., Pohl, M., & Zurita-Heras,  
734 J.-A. 2010, *A&A*, 520, A111+
- 735 Bamba, A., Ueno, M., Koyama, K., & Yamauchi, S. 2003, *ApJ*, 589, 253
- 736 Blandford, R., & Eichler, D. 1987, *Phys. Rep.*, 154, 1
- 737 Castelletti, G., Dubner, G., Golap, K., & Goss, W. M. 2006, *A&A*, 459, 535
- 738 Castro, D., & Slane, P. 2010, *ApJ*, 717, 372
- 739 Dame, T. M. 2011, ArXiv e-prints
- 740 de Geus, E. J., Bronfman, L., & Thaddeus, P. 1990, *A&A*, 231, 137

- 741 Funk, S., Hinton, J. A., Pühlhofer, G., Aharonian, F. A., Hofmann, W., Reimer, O., &  
742 Wagner, S. 2007, *ApJ*, 662, 517
- 743 Gaensler, B. M., Schulz, N. S., Kaspi, V. M., Pivovarov, M. J., & Becker, W. E. 2003, *ApJ*,  
744 588, 441
- 745 Gaisser, T. K., Protheroe, R. J., & Stanev, T. 1998, *ApJ*, 492, 219
- 746 Gotthelf, E. V., & Halpern, J. P. 2008, *ApJ*, 681, 515
- 747 Grenier, I. A., Casandjian, J.-M., & Terrier, R. 2005, *Science*, 307, 1292
- 748 Grondin, M. ., et al. 2011, *ArXiv e-prints*
- 749 Hartman, R. C., et al. 1999, *ApJS*, 123, 79
- 750 Hertz, P., & Grindlay, J. E. 1988, *AJ*, 96, 233
- 751 Hwang, U., Petre, R., & Flanagan, K. A. 2008, *ApJ*, 676, 378
- 752 James, F., & Roos, M. 1975, *Comput. Phys. Commun.*, 10, 343
- 753 Kargaltsev, O., Pavlov, G. G., & Wong, J. A. 2009, *The Astrophysical Journal*, 690, 891
- 754 Katagiri, H., et al. 2011, *ArXiv e-prints*
- 755 Kerr, M. 2011, PhD in physics, University of Washington
- 756 Krause, J., Carmona, E., & Reichardt, I. 2011, in (Presented at the 2011 Fermi Symposium,  
757 Rome Italy)
- 758 Landi, R., de Rosa, A., Dean, A. J., Bassani, L., Ubertini, P., & Bird, A. J. 2007a, *MNRAS*,  
759 380, 926
- 760 Landi, R., Masetti, N., Bassani, L., Cellone, S. A., Romero, G. E., Ubertini, P., & Dean,  
761 A. J. 2007b, *The Astronomer’s Telegram*, 1047, 1
- 762 Landi, R., et al. 2006, *ApJ*, 651, 190
- 763 Malizia, A., et al. 2005, *ApJ*, 630, L157
- 764 Markwardt, C. B., & Ogelman, H. 1995, *Nature*, 375, 40
- 765 Matsumoto, H., et al. 2007, *PASJ*, 59, 199
- 766 —. 2008, *PASJ*, 60, 163

- Mattox, J. R., et al. 1996, *ApJ*, 461, 396
- Mizukami, T., et al. 2011, *ArXiv e-prints*
- Murphy, T., Mauch, T., Green, A., Hunstead, R. W., Piestrzynska, B., Kels, A. P., & Sztajer, P. 2007, *MNRAS*, 382, 382
- Paron, S., Dubner, G., Reynoso, E., & Rubio, M. 2008, *A&A*, 480, 439
- Petre, R., Becker, C. M., & Winkler, P. F. 1996, *ApJ*, 465, L43+
- Pollock, A. M. T. 1985, *A&A*, 150, 339
- Protassov, R., van Dyk, D. A., Connors, A., Kashyap, V. L., & Siemiginowska, A. 2002, *ApJ*, 571, 545
- Reynoso, E. M., Dubner, G. M., Goss, W. M., & Arnal, E. M. 1995, *AJ*, 110, 318
- Reynoso, E. M., Green, A. J., Johnston, S., Dubner, G. M., Giacani, E. B., & Goss, W. M. 2003, *MNRAS*, 345, 671
- Rodriguez, J., Tomsick, J. A., Foschini, L., Walter, R., Goldwurm, A., Corbel, S., & Kaaret, P. 2003, *A&A*, 407, L41
- Rowell, G., Horns, D., Fukui, Y., & Moriguchi, Y. 2008, in *American Institute of Physics Conference Series*, Vol. 1085, *American Institute of Physics Conference Series*, ed. F. A. Aharonian, W. Hofmann, & F. Rieger, 241–244
- Sreekumar, P., et al. 1998, *The Astrophysical Journal*, 494, 523
- Sugizaki, M., Mitsuda, K., Kaneda, H., Matsuzaki, K., Yamauchi, S., & Koyama, K. 2001, *ApJS*, 134, 77
- Swanenburg, B. N., et al. 1981, *ApJ*, 243, L69
- Taylor, A. R., et al. 2003, *AJ*, 125, 3145
- The Fermi-LAT Collaboration. 2010, *ArXiv e-prints*
- The Fermi LAT Collaboration, & Timing Consortium, P. 2010, *ArXiv e-prints*
- The H. E. S. S. Collaboration: S. Funk, Hinton, J. A., & deJager, O. C. 2007, *ArXiv e-prints*
- The H.E.S.S. Collaboration. 2011, The H.E.S.S. Source Catalog, <http://www.mpi-hd.mpg.de/hfm/HESS/pages/home/sources/>

- 794 Tomsick, J. A., Lingenfelter, R., Walter, R., Rodriguez, J., Goldwurm, A., Corbel, S., &  
795 Kaaret, P. 2003, IAU Circ., 8076, 1
- 796 Torii, K., et al. 1998, ApJ, 494, L207+
- 797 Weekes, T. C., et al. 1989, ApJ, 342, 379
- 798 Weinstein, A., & for the VERITAS Collaboration. 2009, ArXiv e-prints
- 799 Young, E. T., Lada, C. J., & Wilking, B. A. 1986, ApJ, 304, L45

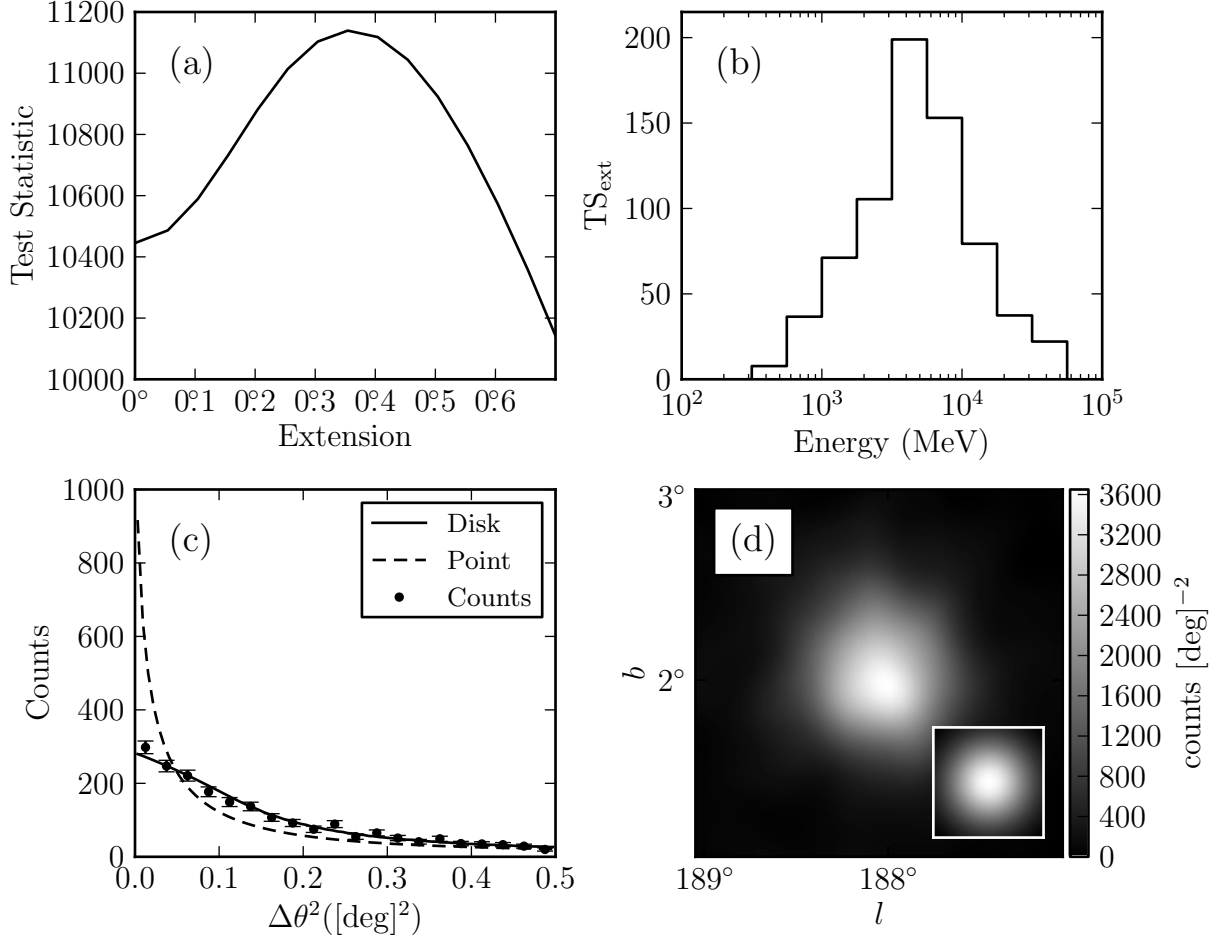


Fig. 1.— Counts and test statistic profiles for the SNR IC443. (a) TS vs. extension of the source. (b)  $TS_{\text{ext}}$  for individual energy bands. (c) observed radial profile of counts in comparison to the expected profiles for a spatially extended source (solid and colored red in the online version) and for a point source (dashed and colored blue in the online version). (d) smoothed count map after subtraction of the diffuse emission compared to the LAT PSF (inset). Plots (a), (c), and (d) use only 1-100 GeV photons. Plots (c) and (d) use only photons which converted in the front part of the tracker and have an improved angular resolution.



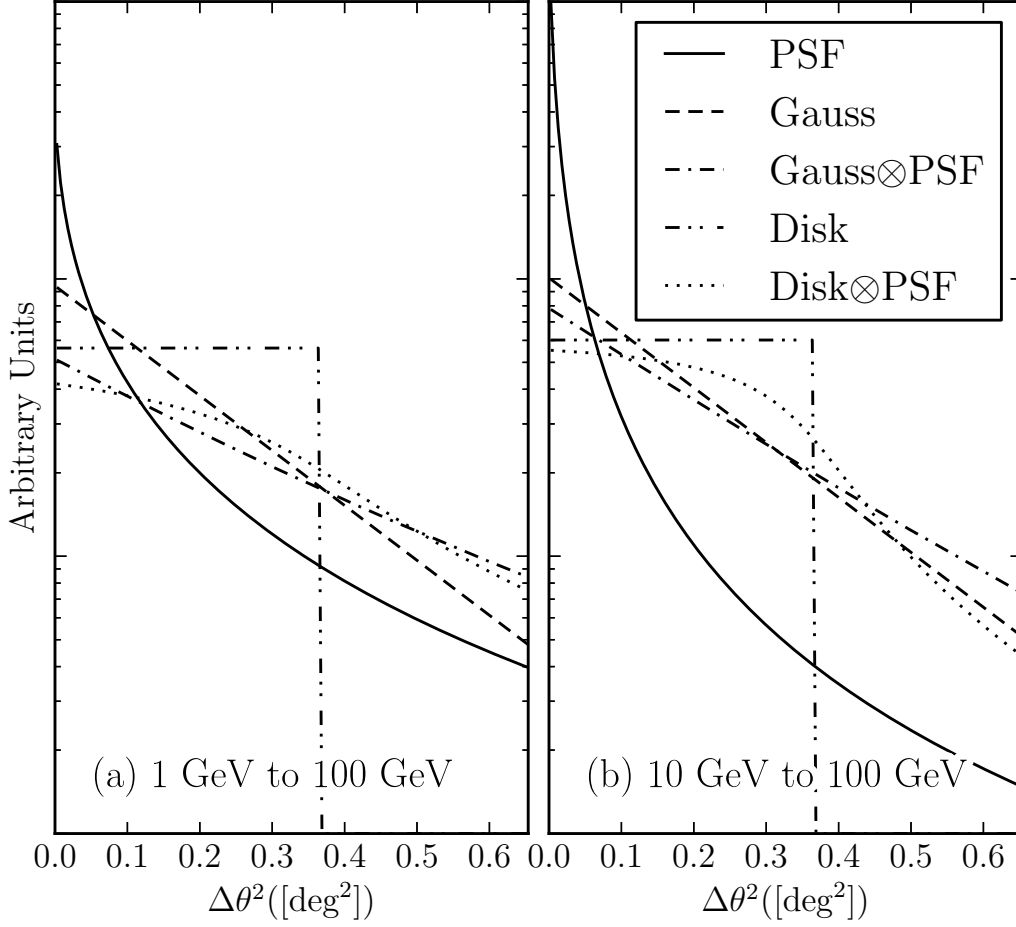


Fig. 2.— A comparison of a Gaussian and disk surface brightness profiles of extended sources before and after convolving with the PSF for two energy ranges. The solid black line is the PSF that would be observed for a power-law source of spectral index 2. The dashed line and the dash-dot line are the brightness profile of a Gaussian with  $r_{68} = 0.5$  and the convolution of this profile with the LAT PSF respectively (colored red in the online version). The dash-dot-dot and the dot-dot line are the brightness profile of a uniform disk with  $r_{68} = 0.5$  and the convolution of this profile with the LAT PSF respectively (colored blue in the online version).

Table 1. Monte Carlo Validation Parameters

| Spectral Index | Flux <sup>(a)</sup><br>(ph cm <sup>-2</sup> s <sup>-1</sup> ) | $N_{\text{sims}}$ | $\langle \text{TS} \rangle$ |
|----------------|---------------------------------------------------------------|-------------------|-----------------------------|
| 1.5            | $10^{-6}$                                                     | 31952             | 92862                       |
|                | $3 \times 10^{-7}$                                            | 31962             | 22169                       |
|                | $10^{-7}$                                                     | 31977             | 5806                        |
|                | $3 \times 10^{-8}$                                            | 31991             | 1270                        |
|                | $10^{-8}$                                                     | 31940             | 301                         |
|                | $3 \times 10^{-9}$                                            | 30324             | 62                          |
| 2              | $10^{-6}$                                                     | 31872             | 22067                       |
|                | $3 \times 10^{-7}$                                            | 31890             | 4898                        |
|                | $10^{-7}$                                                     | 31858             | 1097                        |
|                | $3 \times 10^{-8}$                                            | 31632             | 236                         |
|                | $10^{-8}$                                                     | 27491             | 103                         |
| 2.5            | $10^{-6}$                                                     | 31822             | 4706                        |
|                | $3 \times 10^{-7}$                                            | 31822             | 889                         |
|                | $10^{-7}$                                                     | 31169             | 176                         |
|                | $3 \times 10^{-8}$                                            | 21591             | 41                          |
| 3              | $10^{-6}$                                                     | 31763             | 929                         |
|                | $3 \times 10^{-7}$                                            | 31665             | 161                         |
|                | $10^{-7}$                                                     | 19271             | 40                          |

<sup>(a)</sup>Integral 1-100 MeV flux.

Note. — the spectral models used in the Monte Carlo validation of `pointlike`. For each model, the number of statistically independent simulations and the average value of TS is tabulated. The models spans representative spectral parameters.

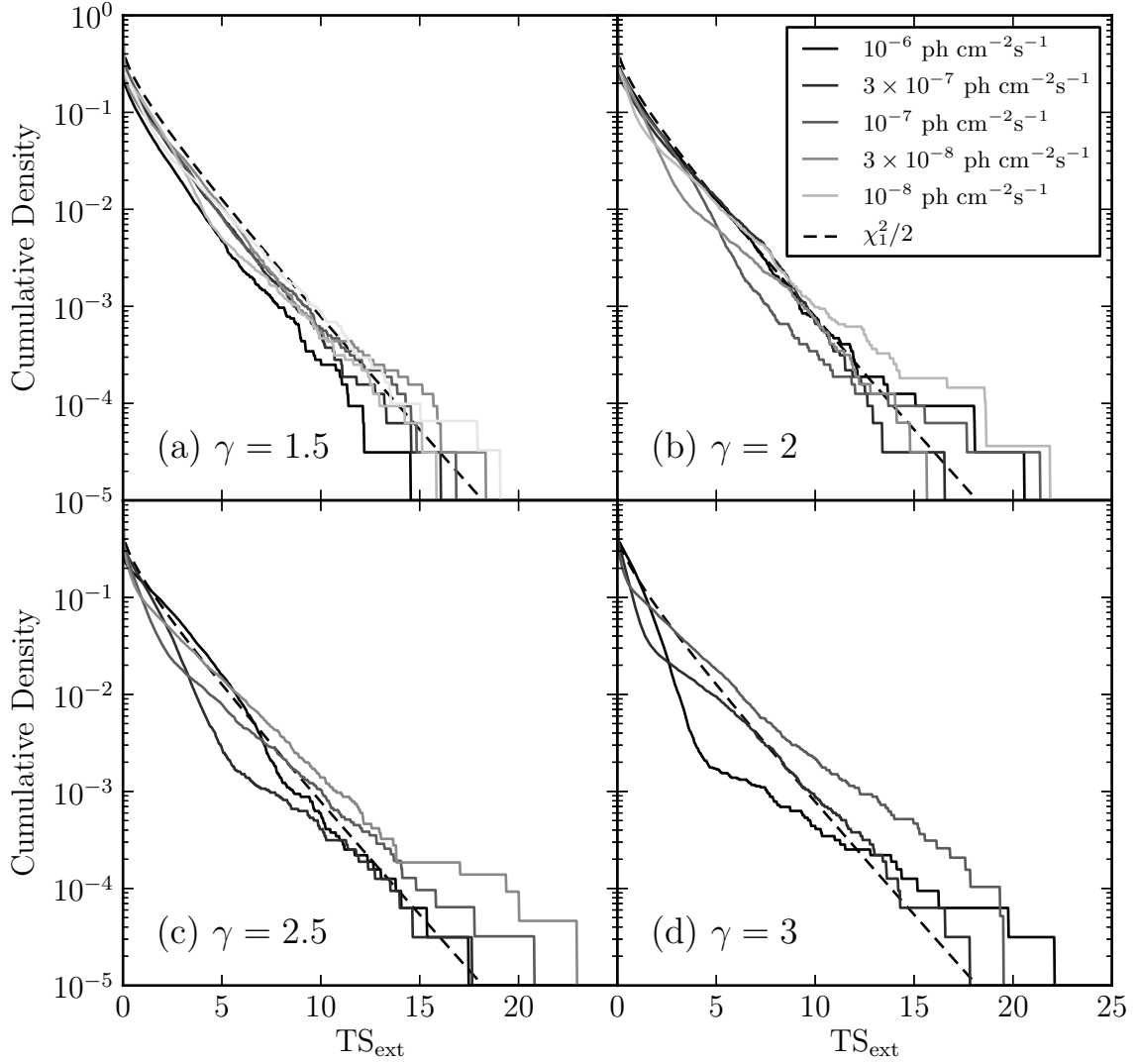


Fig. 3.— Distribution of the test statistic  $TS_{\text{ext}}$  of a likelihood ratio test when fitting the extension of a point source. The four plots represent simulated point sources of different spectral indices and the different lines (colored in the online version) represent point sources with different 100 MeV to 100 GeV integral fluxes. The dashed line (colored red in online version) is the cumulative density function of Equation 9.

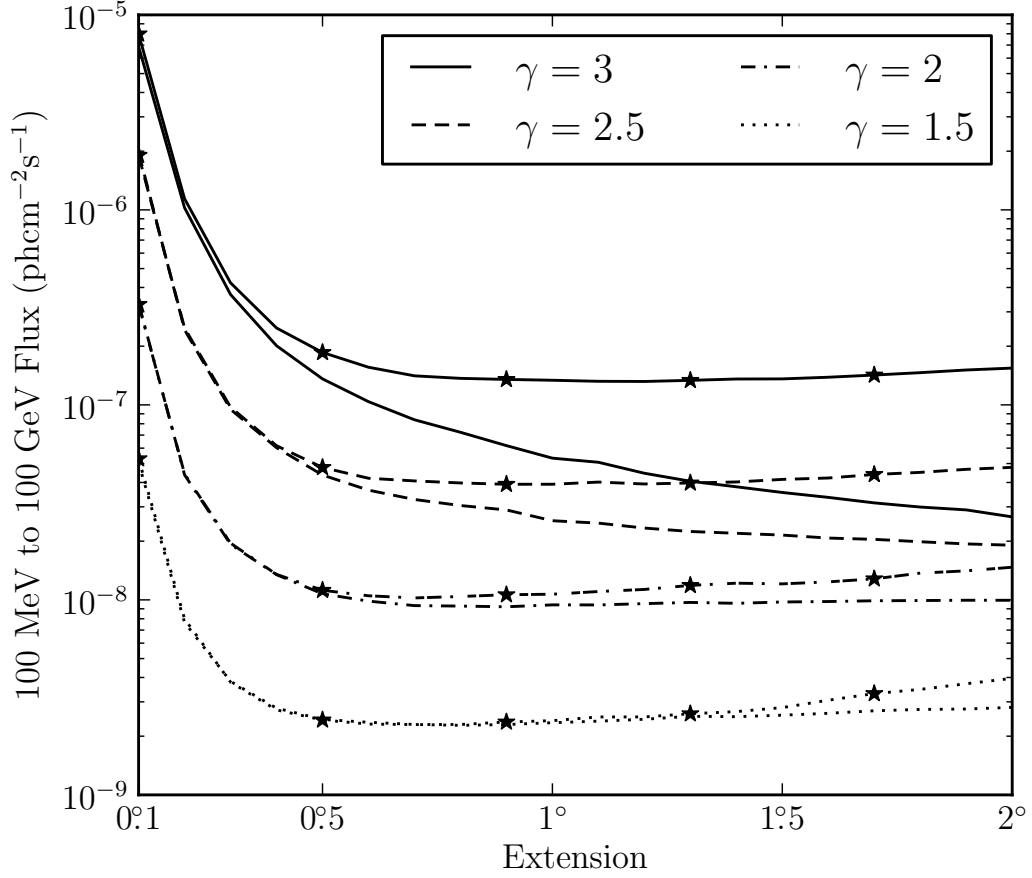


Fig. 4.— The detection threshold ( $\langle TS_{\text{ext}} \rangle = 16$ ) to resolve a uniform disk extended source for a two-year exposure. All sources have an assumed power-law spectrum and the different colors correspond to different simulated spectral indices. The solid line is the detection threshold using photons with energy between 100 MeV and 100 GeV while the dashed line is the threshold using 1-100 GeV photons.

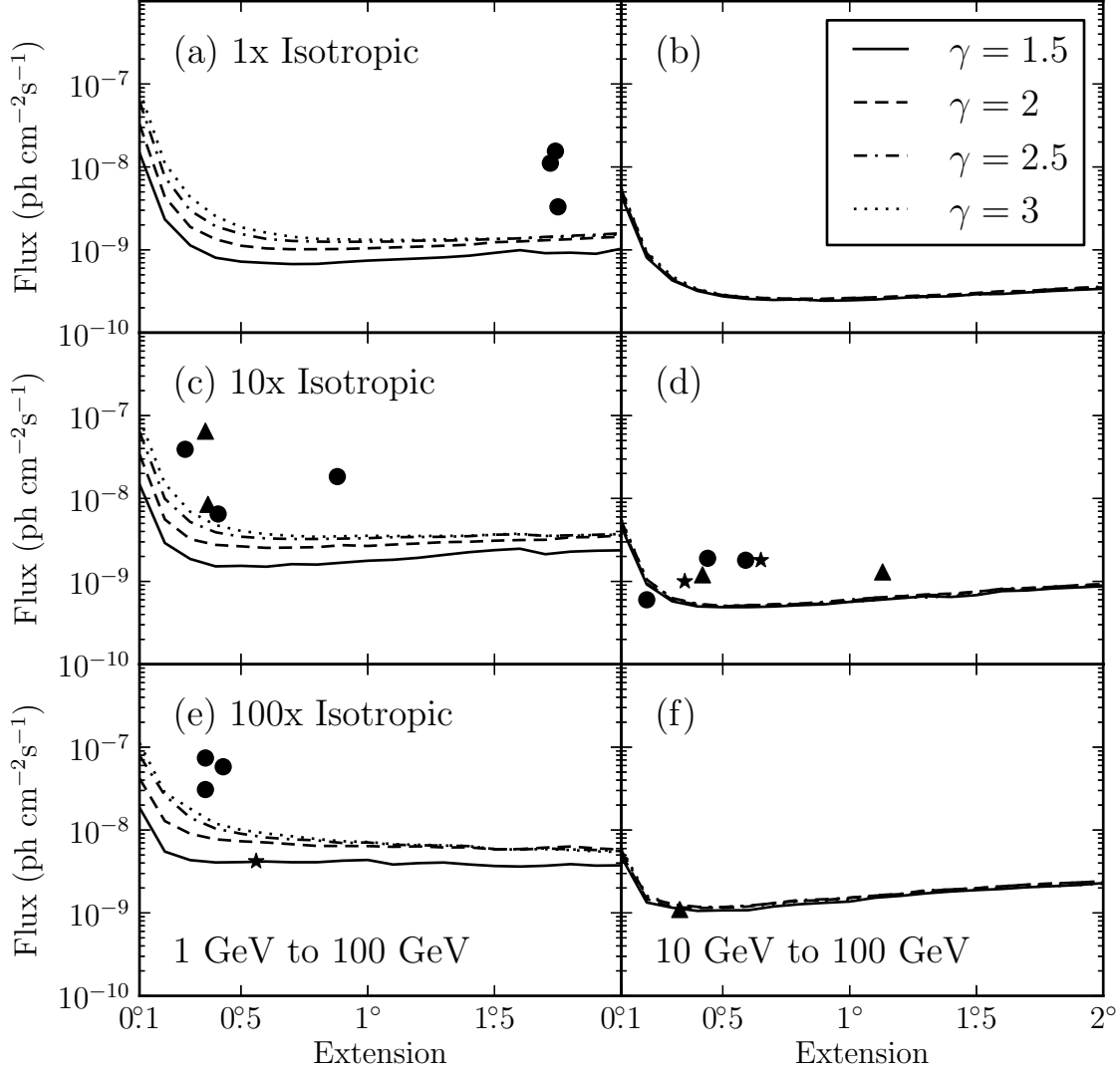


Fig. 5.— the LAT detection threshold for four spectral indices and three background (1x, 10x, and 100x the Sreekumar-like isotropic spectrum) for a two-year exposure. The left plots are the detection threshold when using 1-100 GeV photons and the right plots are the detection threshold when using 10-100 GeV photons. The flux is integrated only in the selected energy range. Overlaid on this plot are the LAT detected extended sources placed by the magnitude of the nearby Galactic diffuse emission and the energy range they were analyzed with. The stars (colored red in the electronic version) are sources with a spectral index closer to 1.5, the triangles (colored blue) an index closer to 2, and the circles (colored green) an index closer to 2.5. The circle in plot (d) below the sensitivity line is MSH 15-52 which was found by our analysis to have  $TS_{\text{ext}} = 6.5$ .

Table 2. Extension Detection Threshold

| $\gamma$ | BG   | 0.1    | 0.2   | 0.3   | 0.4   | 0.5   | 0.6  | 0.7  | 0.8  | 0.9  | 1.0  | 1.1  | 1.2  | 1.3  | 1.4  | 1.5  | 1.6  | 1.7  | 1.8  | 1.9  | 2.0  |
|----------|------|--------|-------|-------|-------|-------|------|------|------|------|------|------|------|------|------|------|------|------|------|------|------|
| E>1 GeV  |      |        |       |       |       |       |      |      |      |      |      |      |      |      |      |      |      |      |      |      |      |
| 1.5      | x1   | 148.1  | 23.3  | 11.3  | 8.0   | 7.2   | 6.9  | 6.7  | 6.8  | 7.1  | 7.4  | 7.6  | 7.9  | 8.1  | 8.5  | 9.2  | 9.9  | 9.1  | 9.2  | 9.0  | 10.3 |
|          | x10  | 148.4  | 29.0  | 18.7  | 15.2  | 15.4  | 15.0 | 16.1 | 16.0 | 16.8 | 17.7 | 18.2 | 19.3 | 20.9 | 22.5 | 23.8 | 24.8 | 21.3 | 22.8 | 23.4 | 23.7 |
|          | x100 | 186.8  | 55.0  | 43.4  | 40.7  | 41.0  | 41.8 | 40.9 | 40.9 | 42.7 | 43.6 | 38.4 | 39.9 | 40.6 | 38.4 | 36.9 | 36.3 | 37.1 | 38.8 | 37.2 | 37.6 |
| 2        | x1   | 328.4  | 43.4  | 18.9  | 13.4  | 11.2  | 10.4 | 10.2 | 10.2 | 10.2 | 10.4 | 10.7 | 10.9 | 11.2 | 11.5 | 12.4 | 12.6 | 13.0 | 13.4 | 14.0 | 14.4 |
|          | x10  | 341.0  | 55.9  | 32.3  | 27.6  | 26.5  | 25.4 | 25.6 | 25.9 | 27.4 | 26.8 | 27.8 | 28.7 | 29.8 | 30.1 | 31.0 | 31.5 | 31.7 | 34.0 | 34.3 | 35.9 |
|          | x100 | 420.5  | 128.3 | 90.2  | 77.3  | 73.3  | 70.8 | 67.5 | 64.3 | 64.2 | 64.1 | 62.8 | 63.6 | 61.7 | 61.9 | 58.4 | 59.0 | 61.4 | 63.3 | 60.1 | 58.1 |
| 2.5      | x1   | 627.1  | 75.6  | 29.8  | 19.3  | 15.5  | 13.5 | 12.8 | 12.6 | 12.5 | 12.5 | 12.6 | 12.9 | 12.9 | 13.1 | 13.5 | 13.7 | 14.3 | 14.8 | 15.2 | 15.8 |
|          | x10  | 638.9  | 99.1  | 52.1  | 39.1  | 34.6  | 33.0 | 32.5 | 32.5 | 32.8 | 33.2 | 34.1 | 34.3 | 34.5 | 35.1 | 36.6 | 36.9 | 35.5 | 36.0 | 36.5 | 37.3 |
|          | x100 | 795.0  | 262.1 | 140.9 | 104.3 | 90.4  | 81.2 | 77.2 | 75.1 | 69.7 | 70.9 | 66.5 | 65.6 | 64.9 | 64.0 | 58.9 | 58.1 | 60.2 | 58.4 | 57.5 | 55.8 |
| 3        | x1   | 841.5  | 110.6 | 43.2  | 25.5  | 18.7  | 16.1 | 14.4 | 13.6 | 13.3 | 13.2 | 13.1 | 13.1 | 13.4 | 13.6 | 13.5 | 13.8 | 14.2 | 14.4 | 14.8 | 15.4 |
|          | x10  | 921.6  | 151.3 | 69.1  | 47.8  | 40.7  | 37.1 | 35.5 | 34.5 | 35.1 | 35.5 | 35.3 | 35.3 | 35.4 | 35.5 | 36.8 | 37.6 | 35.3 | 35.4 | 36.3 | 36.6 |
|          | x100 | 1124.1 | 282.9 | 181.1 | 119.8 | 100.7 | 91.1 | 84.3 | 77.9 | 73.3 | 71.8 | 67.6 | 66.4 | 65.5 | 63.9 | 59.0 | 58.6 | 58.8 | 57.5 | 55.4 | 54.4 |
| E>10 GeV |      |        |       |       |       |       |      |      |      |      |      |      |      |      |      |      |      |      |      |      |      |
| 1.5      | x1   | 44.6   | 8.0   | 4.3   | 3.2   | 2.7   | 2.6  | 2.5  | 2.5  | 2.4  | 2.5  | 2.5  | 2.6  | 2.7  | 2.8  | 2.9  | 2.9  | 3.1  | 3.2  | 3.3  | 3.4  |
|          | x10  | 45.2   | 9.2   | 5.8   | 5.0   | 4.9   | 4.9  | 5.0  | 5.2  | 5.3  | 5.7  | 5.9  | 6.3  | 6.6  | 6.5  | 6.8  | 7.6  | 7.8  | 8.2  | 8.5  | 8.7  |
|          | x100 | 47.3   | 13.4  | 11.6  | 10.6  | 10.8  | 10.8 | 12.0 | 12.7 | 13.2 | 13.7 | 15.3 | 16.1 | 17.2 | 18.2 | 18.9 | 19.5 | 20.4 | 21.0 | 21.7 | 22.9 |
| 2        | x1   | 49.7   | 8.4   | 4.4   | 3.3   | 2.8   | 2.6  | 2.6  | 2.6  | 2.6  | 2.6  | 2.7  | 2.7  | 2.8  | 2.9  | 3.0  | 3.2  | 3.2  | 3.4  | 3.5  | 3.5  |
|          | x10  | 48.6   | 9.5   | 6.0   | 5.2   | 5.0   | 5.2  | 5.2  | 5.3  | 5.4  | 5.8  | 6.4  | 6.6  | 7.0  | 7.1  | 7.5  | 8.0  | 8.3  | 8.6  | 9.0  | 9.2  |
|          | x100 | 51.8   | 14.7  | 11.8  | 11.5  | 11.5  | 11.9 | 13.2 | 14.0 | 14.3 | 15.3 | 16.2 | 16.9 | 18.4 | 19.2 | 19.8 | 21.0 | 22.0 | 22.8 | 23.2 | 24.3 |
| 2.5      | x1   | 53.1   | 9.1   | 4.5   | 3.3   | 2.8   | 2.7  | 2.6  | 2.5  | 2.5  | 2.6  | 2.7  | 2.7  | 2.8  | 2.8  | 2.9  | 3.1  | 3.2  | 3.3  | 3.5  | 3.6  |
|          | x10  | 53.7   | 10.5  | 6.3   | 5.4   | 5.1   | 5.1  | 5.3  | 5.4  | 5.7  | 6.0  | 6.3  | 6.6  | 6.8  | 6.9  | 7.5  | 8.1  | 8.3  | 8.6  | 8.9  | 9.2  |
|          | x100 | 57.0   | 15.6  | 12.7  | 11.9  | 11.8  | 12.2 | 13.1 | 14.3 | 14.6 | 15.2 | 16.3 | 17.0 | 18.8 | 19.2 | 19.9 | 21.0 | 21.9 | 22.3 | 23.3 | 23.7 |
| 3        | x1   | 55.5   | 9.4   | 4.8   | 3.4   | 2.9   | 2.7  | 2.6  | 2.5  | 2.5  | 2.5  | 2.6  | 2.7  | 2.7  | 2.8  | 2.9  | 3.0  | 3.1  | 3.2  | 3.4  | 3.4  |
|          | x10  | 56.0   | 10.5  | 6.2   | 5.3   | 5.1   | 5.1  | 5.1  | 5.3  | 5.5  | 5.7  | 5.9  | 6.4  | 6.4  | 6.6  | 7.0  | 7.8  | 8.0  | 8.3  | 8.6  | 8.9  |
|          | x100 | 60.3   | 16.2  | 12.7  | 11.7  | 11.8  | 12.2 | 12.6 | 13.8 | 14.2 | 14.6 | 15.8 | 16.5 | 17.6 | 18.5 | 19.4 | 19.8 | 20.7 | 21.0 | 21.8 | 22.5 |

Note. — The detection threshold to resolve a uniform disk spatially extended sources using two years of data for sources of varying energy ranges, spectral indices, and background levels. The extended sources were simulated against a Sreekumar-like isotropic spectrum and the second column is the factor that the simulated background was scaled by. The remaining columns are varying sizes of the source in degrees assuming a uniform surface brightness. The table quotes integral fluxes in the analyzed energy range (1-100 GeV or 10-100 GeV) in units of  $10^{-10} \text{ph cm}^{-2} \text{s}^{-1}$ .

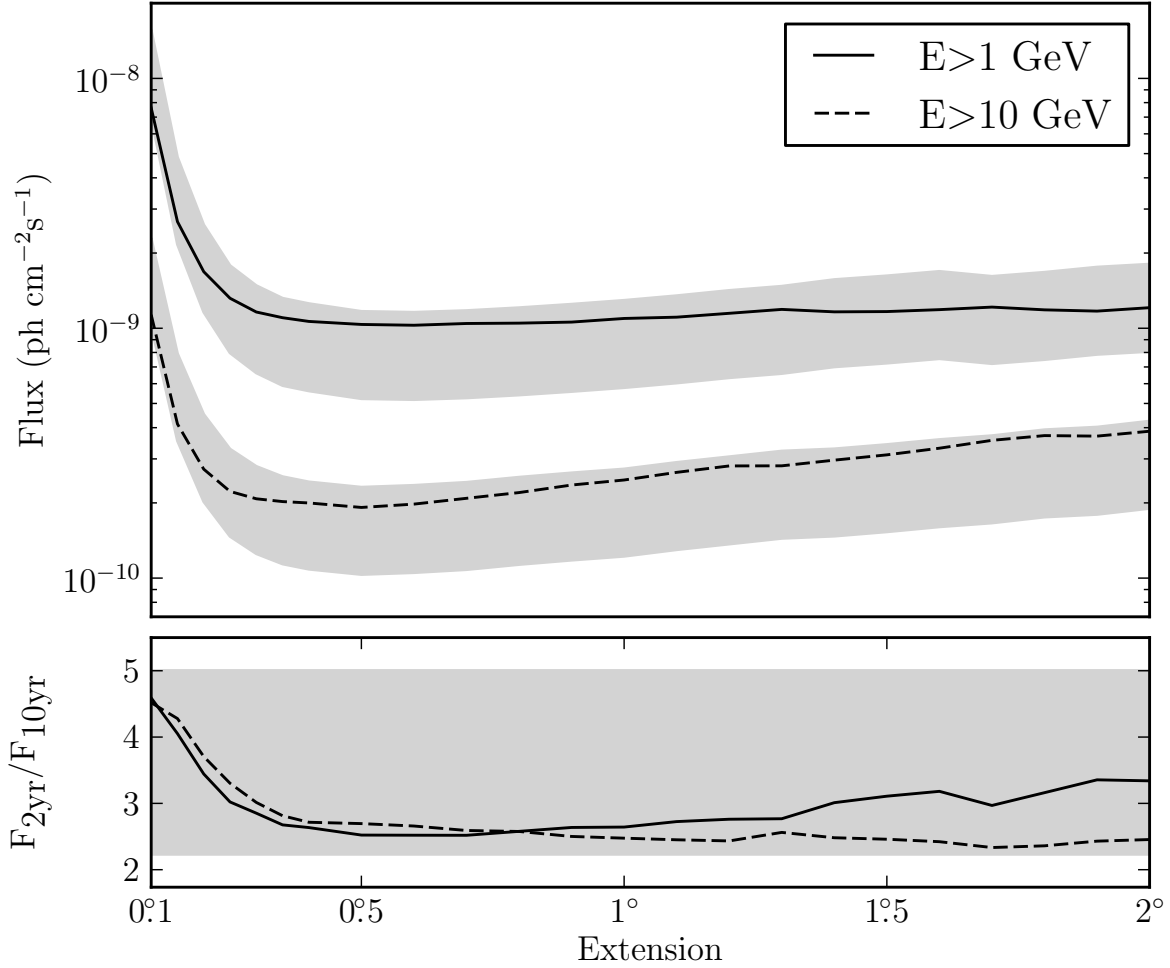


Fig. 6.— The LAT’s projected detection threshold to extension after 10 years for a power-law source of spectral index 2 against 10 times the isotropic background in the energy range from 1 GeV to 100 GeV (solid line colored red in the electronic version) and 10 GeV to 100 GeV (dashed line colored blue in the electronic version). The solid gray region is the detection threshold assuming the sensitivity improves from 2 to 10 years by the square root of time (top edge) and linearly with time (bottom edge). The lower plot shows the factor increase in sensitivity. For small extended sources, our detection threshold to the extension of a source will improve by a factor better than the square root of time.



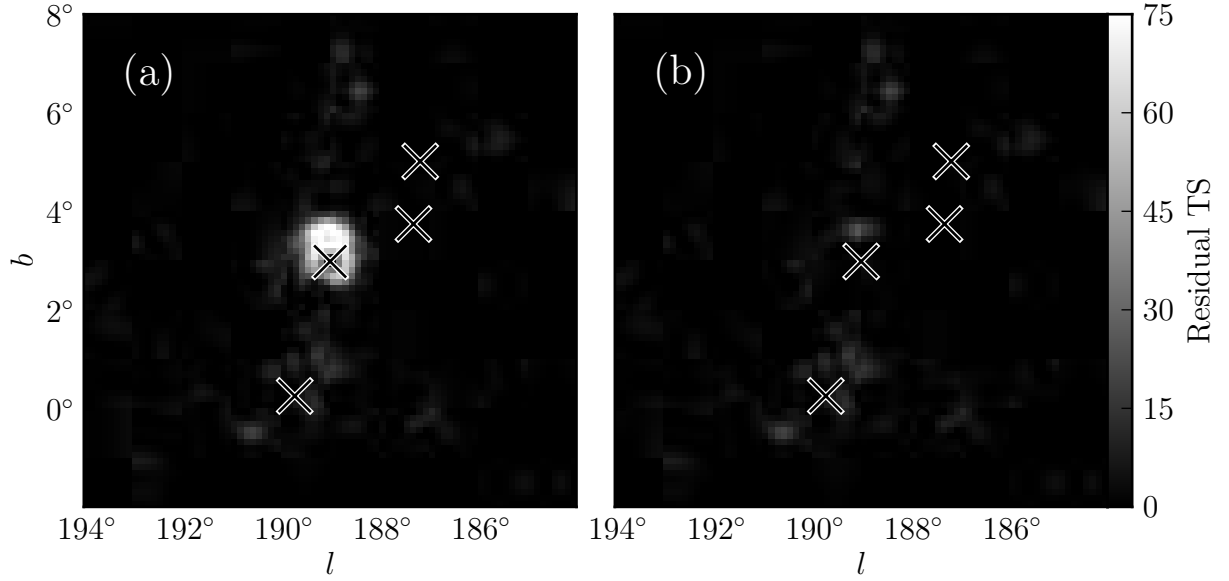


Fig. 7.— A test statistic map generated for the region around the SNR IC443 using 1-100 GeV photons. (a) test statistic map after subtracting IC443 modeled as a point source. (b) same as (a), but IC443 modeled as extended source. Crosses represent sources included in the model of the region. Such maps were generated for all extended source candidates.

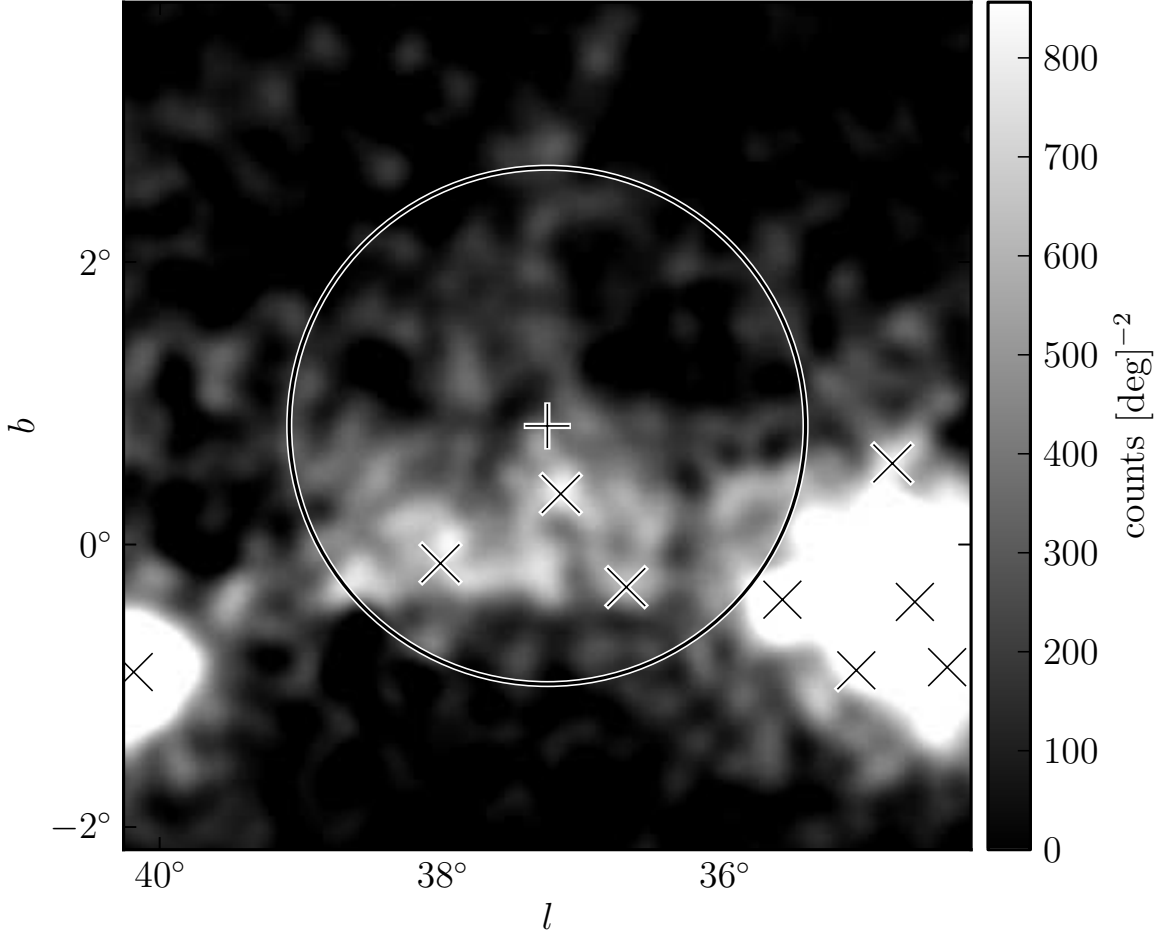


Fig. 8.— A diffuse-emission-subtracted 1-100 GeV counts map of the region around 2FGL J1856.2+0450c smoothed by a  $0.1^\circ$  Gaussian kernel. The plus and circle (colored red in the online version) represent the center and size of the best fit radially symmetric source with a uniform intensity profile. The black crosses represent the position of background 2FGL sources. The result is statistically significant, but the extension encompasses many catalog sources and the emission does not look to be uniform. Instead, this source is probably fitting large-scale diffuse residual features. Although the fit is statistically significant, it likely corresponds to residual features of inaccurately modeled diffuse emission picked up by the fit. We manually discard candidates that appear like this.

Table 3. Extension fit for the twelve extended sources included in 2FGL

| Name           | GLON<br>(deg.) | GLAT<br>(deg.) | $\sigma$<br>(deg.)       | TS      | TS <sub>ext</sub> | Pos Err<br>(deg.) | Flux <sup>(a)</sup><br>(ph cm <sup>-2</sup> s <sup>-1</sup> ) | Index           |
|----------------|----------------|----------------|--------------------------|---------|-------------------|-------------------|---------------------------------------------------------------|-----------------|
| E>1 GeV        |                |                |                          |         |                   |                   |                                                               |                 |
| SMC            | 302.68         | -44.81         | $1.75 \pm 0.07 \pm 0.02$ | 94.8    | 67.4              | 0.12              | $3.3 \pm 0.4$                                                 | $2.41 \pm 0.17$ |
| LMC            | 279.10         | -32.61         | $1.74 \pm 0.05 \pm 0.13$ | 1101.3  | 860.5             | 0.05              | $15.5 \pm 0.6$                                                | $2.48 \pm 0.06$ |
| IC443          | 189.05         | 3.04           | $0.36 \pm 0.01 \pm 0.04$ | 10719.8 | 510.4             | 0.01              | $64.8 \pm 1.2$                                                | $2.23 \pm 0.02$ |
| Vela X         | 263.34         | -3.11          | 0.88                     |         |                   |                   |                                                               |                 |
| Centarus A     | 309.52         | 19.42          | $\sim 10$                |         |                   |                   |                                                               |                 |
| W28            | 6.50           | -0.27          | $0.43 \pm 0.02 \pm 0.03$ | 1324.8  | 177.4             | 0.01              | $58.0 \pm 1.8$                                                | $2.63 \pm 0.03$ |
| W30            | 8.61           | -0.20          | $0.36 \pm 0.02 \pm 0.02$ | 465.4   | 73.3              | 0.02              | $30.7 \pm 1.6$                                                | $2.59 \pm 0.04$ |
| W44            | 34.69          | -0.38          | $0.36 \pm 0.01 \pm 0.02$ | 1903.3  | 217.7             | 0.01              | $73.6 \pm 1.8$                                                | $2.68 \pm 0.02$ |
| W51C           | 49.13          | -0.45          | $0.28 \pm 0.02 \pm 0.05$ | 1819.5  | 115.7             | 0.01              | $39.3 \pm 1.3$                                                | $2.35 \pm 0.03$ |
| Cygnus Loop    | 74.22          | -8.46          | $1.72 \pm 0.05 \pm 0.07$ | 356.5   | 356.5             | 0.06              | $11.1 \pm 0.7$                                                | $2.53 \pm 0.11$ |
| E>10 GeV       |                |                |                          |         |                   |                   |                                                               |                 |
| MSH 15-52      | 320.38         | -1.22          | $0.20 \pm 0.04 \pm 0.03$ | 76.2    | 6.5               | 0.03              | $0.6 \pm 0.7$                                                 | $2.27 \pm 0.73$ |
| HESS J1825-137 | 17.56          | -0.46          | $0.65 \pm 0.03 \pm 0.01$ | 83.6    | 55.9              | 0.05              | $1.8 \pm 0.2$                                                 | $1.74 \pm 0.19$ |

<sup>(a)</sup>Integrated in the fit energy range (either 1-100 GeV or 10-100 GeV).

Note. — All sources were fit using a spatial model assuming a uniform radially symmetric intensity distribution. GLON and GLAT are Galactic longitude and latitude of the best fit extended source respectively. The first error on  $\sigma$  is statistical and the second is systematic (see Section 5.2). Pos Err is the error on the position of the source. Vela X and the Centarus A Lobes were not fit by our analysis but are include for completeness.

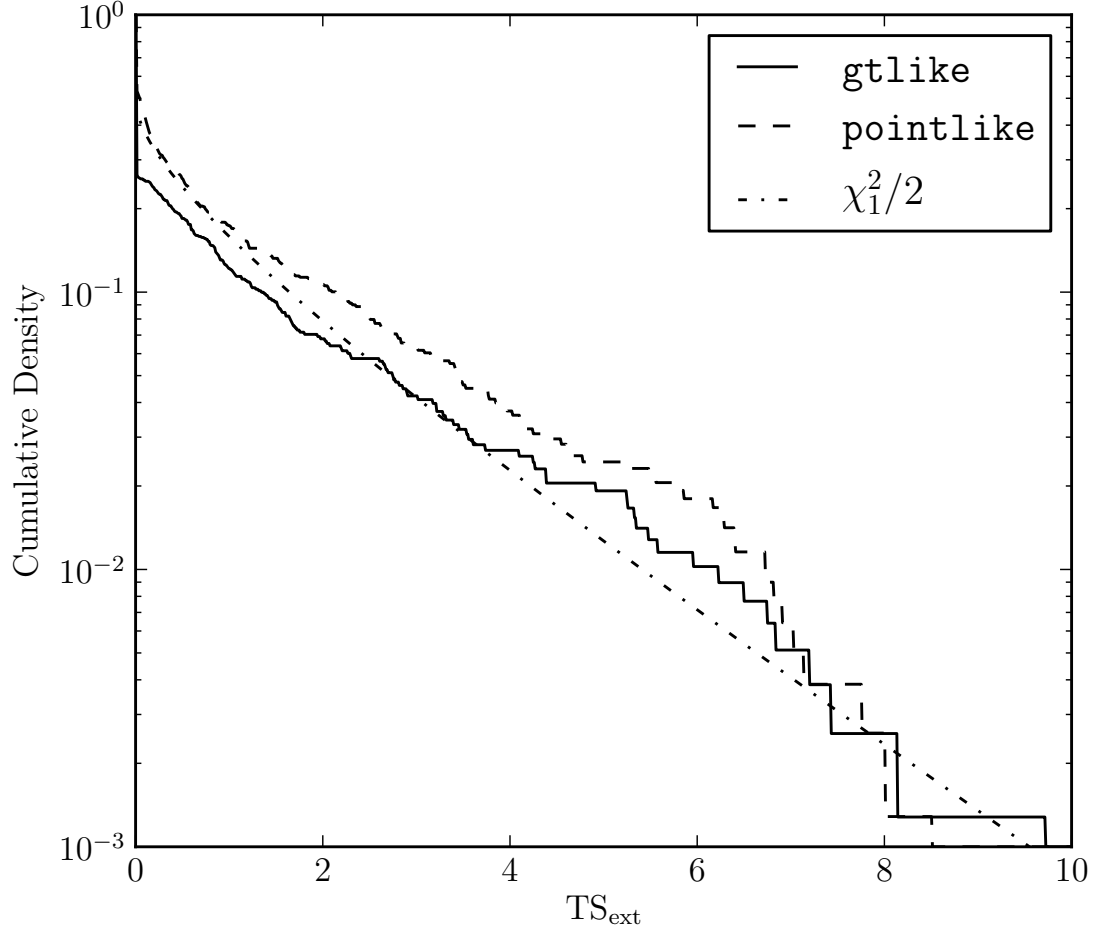


Fig. 9.— The cumulative density of  $TS_{\text{ext}}$  for 783 of the clean AGN in 2LAC which are significant above 1 GeV calculated with **pointlike** (the dashed line colored blue in the electronic version) and with **gtlike** (the solid line colored red in the electronic version). AGNs are too far and too small to be resolved by the LAT. Therefore, the cumulative density of  $TS_{\text{ext}}$  is expected to follow a  $\chi^2/2$  distribution (Equation 9) and is the dash-dotted line (colored red in the electronic version).

Table 4. Extension fit for the nine new extended sources

| Name               | GLON<br>(deg.) | GLAT<br>(deg.) | $\sigma$<br>(deg.)       | TS    | TS <sub>ext</sub> | Pos Err<br>(deg.) | Flux <sup>(a)</sup><br>(ph cm <sup>-2</sup> s <sup>-1</sup> ) | Index           | Counterpart     |
|--------------------|----------------|----------------|--------------------------|-------|-------------------|-------------------|---------------------------------------------------------------|-----------------|-----------------|
| E>1 GeV            |                |                |                          |       |                   |                   |                                                               |                 |                 |
| 2FGL J0823.0-4246  | 260.32         | -3.28          | $0.37 \pm 0.03 \pm 0.02$ | 320.9 | 46.3              | 0.02              | $8.5 \pm 0.7$                                                 | $2.20 \pm 0.09$ | Puppis A        |
| 2FGL J1627.0-2425c | 353.08         | 16.78          | $0.41 \pm 0.05 \pm 0.02$ | 144.5 | 31.1              | 0.04              | $6.5 \pm 0.6$                                                 | $2.49 \pm 0.14$ | Ophiuchus       |
| 2FGL J1712.4-3941  | 347.25         | -0.54          | $0.56 \pm 0.04 \pm 0.01$ | 75.0  | 39.6              | 0.05              | $4.2 \pm 0.9$                                                 | $1.47 \pm 0.12$ | RX J1713.7-3946 |
| E>10 GeV           |                |                |                          |       |                   |                   |                                                               |                 |                 |
| 2FGL J0851.7-4635  | 266.29         | -1.43          | $1.13 \pm 0.08 \pm 0.05$ | 116.1 | 87.2              | 0.07              | $1.3 \pm 0.2$                                                 | $1.76 \pm 0.21$ | Vela Jr.        |
| 2FGL J1615.0-5051  | 332.38         | -0.14          | $0.33 \pm 0.04 \pm 0.01$ | 53.4  | 16.3              | 0.04              | $1.1 \pm 0.2$                                                 | $2.24 \pm 0.28$ | HESS J1616-508  |
| 2FGL J1615.2-5138  | 331.66         | -0.66          | $0.42 \pm 0.03 \pm 0.01$ | 76.6  | 48.0              | 0.05              | $1.2 \pm 0.2$                                                 | $1.77 \pm 0.24$ | HESS J1614-518  |
| 2FGL J1632.4-4753c | 336.41         | 0.22           | $0.44 \pm 0.04 \pm 0.03$ | 127.8 | 64.5              | 0.04              | $1.9 \pm 0.2$                                                 | $2.29 \pm 0.21$ | HESS J1632-478  |
| 2FGL J1837.3-0700c | 25.08          | 0.13           | $0.35 \pm 0.08 \pm 0.03$ | 46.2  | 18.8              | 0.07              | $1.0 \pm 0.2$                                                 | $1.63 \pm 0.29$ | HESS J1837-069  |
| 2FGL J2021.5+4026  | 78.18          | 2.19           | $0.59 \pm 0.03 \pm 0.02$ | 222.2 | 116.4             | 0.04              | $1.8 \pm 0.2$                                                 | $2.31 \pm 0.19$ | $\gamma$ -Cygni |

<sup>(a)</sup>Integrated in the fit energy range (either 1-100 GeV or 10-100 GeV).

Note. — The columns in this table are equivalent to the columns in Table 3.

Table 5. Dual localization, alternative PSF, and alternative diffuse results

| Name               | TS <sub>pointlike</sub> | TS <sub>gtlike</sub> | TS <sub>alt,diff</sub> | TS <sub>extpointlike</sub> | TS <sub>extgtlike</sub> | TS <sub>extalt,diff</sub> | $\sigma$<br>(deg.) | $\sigma_{\text{alt,diff}}$<br>(deg.) | $\sigma_{\text{alt,psf}}$<br>(deg.) | TS <sub>inc</sub> |
|--------------------|-------------------------|----------------------|------------------------|----------------------------|-------------------------|---------------------------|--------------------|--------------------------------------|-------------------------------------|-------------------|
| E>1 GeV            |                         |                      |                        |                            |                         |                           |                    |                                      |                                     |                   |
| 2FGL J0823.0-4246  | 350.9                   | 320.9                | 352.5                  | 66.0                       | 46.3                    | 53.6                      | 0.37               | 0.39                                 | 0.38                                | 22.1              |
| 2FGL J1627.0-2425c | 170.2                   | 144.5                | 112.6                  | 43.9                       | 31.1                    | 23.9                      | 0.41               | 0.40                                 | 0.39                                | 20.0              |
| 2FGL J1712.4-3941  | 80.9                    | 75.0                 | 43.4                   | 47.4                       | 39.6                    | 22.2                      | 0.56               | 0.56                                 | 0.54                                | 6.4               |
| E>10 GeV           |                         |                      |                        |                            |                         |                           |                    |                                      |                                     |                   |
| 2FGL J0851.7-4635  | 116.7                   | 116.1                | 122.3                  | 87.1                       | 87.2                    | 90.4                      | 1.13               | 1.16                                 | 1.17                                | 16.1              |
| 2FGL J1615.0-5051  | 52.4                    | 53.4                 | 55.6                   | 17.5                       | 16.3                    | 17.4                      | 0.33               | 0.32                                 | 0.32                                | 11.9              |
| 2FGL J1615.2-5138  | 76.3                    | 76.6                 | 86.3                   | 44.0                       | 48.0                    | 52.6                      | 0.42               | 0.43                                 | 0.43                                | 37.0              |
| 2FGL J1632.4-4753c | 126.6                   | 127.8                | 120.7                  | 63.9                       | 64.5                    | 64.1                      | 0.44               | 0.44                                 | 0.47                                | 40.6              |
| 2FGL J1837.3-0700c | 45.4                    | 46.2                 | 39.0                   | 18.5                       | 18.8                    | 16.6                      | 0.35               | 0.34                                 | 0.38                                | 12.6              |
| 2FGL J2021.5+4026  | 234.3                   | 222.2                | 235.6                  | 135.9                      | 116.4                   | 121.4                     | 0.59               | 0.60                                 | 0.60                                | 24.3              |

Note. — TS<sub>pointlike</sub>, TS<sub>gtlike</sub>, and TS<sub>alt,diff</sub> are the test statistic values from **pointlike**, **gtlike**, and with the alternate diffuse model respectively. TS<sub>extpointlike</sub>, TS<sub>extgtlike</sub>, and TS<sub>extalt,diff</sub> are the test statistic values of the extension test from **pointlike**, **gtlike**, and with the alternate diffuse model respectively.  $\sigma$ ,  $\sigma_{\text{alt,diff}}$ , and  $\sigma_{\text{alt,psf}}$  are the fit extension with the standard analysis, alternate diffuse model, and alternate PSF respectively. TS<sub>inc</sub> is the test statistic for the two point source test.

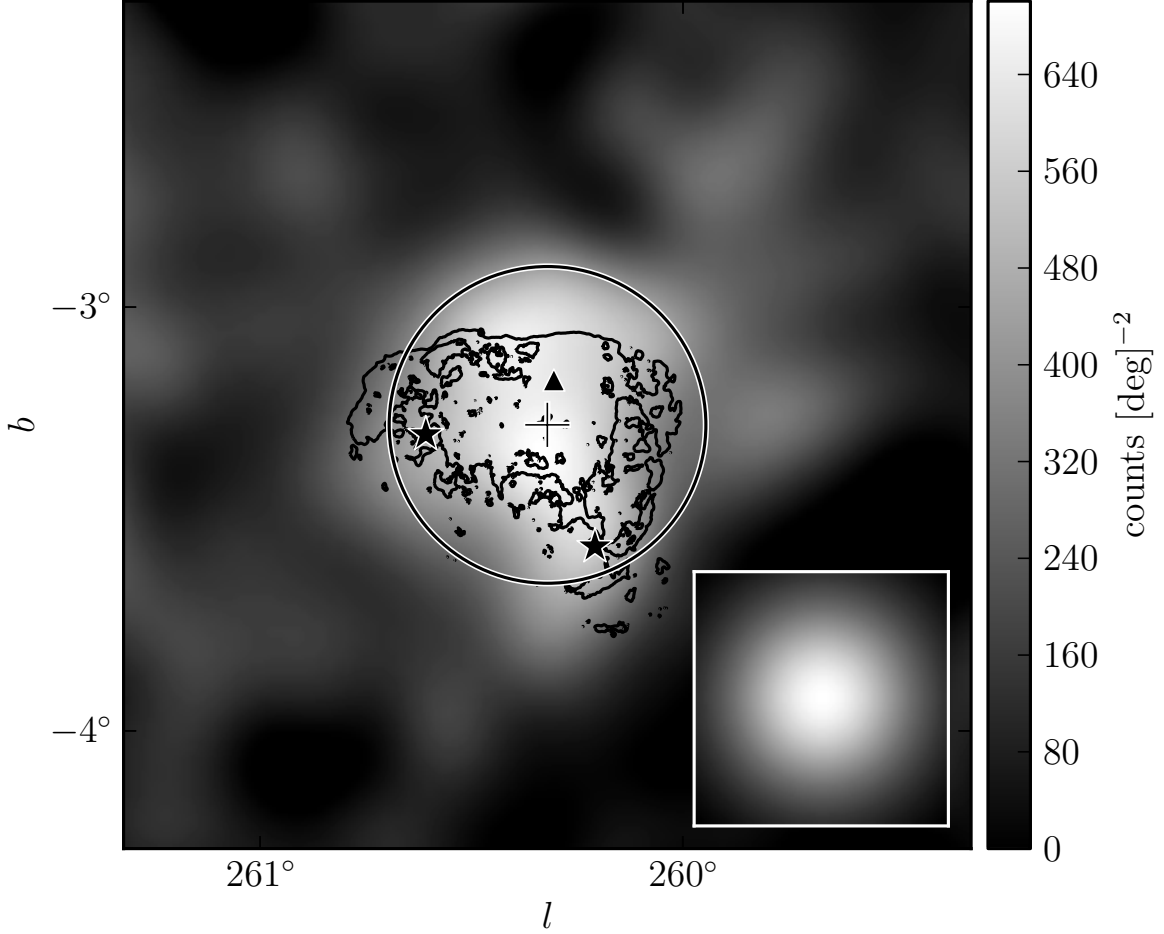


Fig. 10.— A diffuse-emission-subtracted 1 GeV to 100 GeV counts map of the region around 2FGL J0823.0-4246 smoothed by a  $0.1^\circ$  Gaussian kernel. The triangle (colored red in the online version) is the 2FGL position of this source. The cross and circle (colored red) are the best fit position and extension of this source assuming a radially symmetric uniform surface brightness. The two stars (colored green) are the positions of the sources 2FGL J0823.4-4305 and 2FGL J0821.0-4254 which were removed because they are part of the extended source. The lower right inset is the model predicted emission from a point source with the same spectrum as 2FGL J0823.4-4305 smoothed by the same Gaussian kernel. This source is spatially coincident with the Puppis A SNR. The light blue contours correspond to the X-ray image of Puppis A observed by *ROSAT* (Petre et al. 1996).



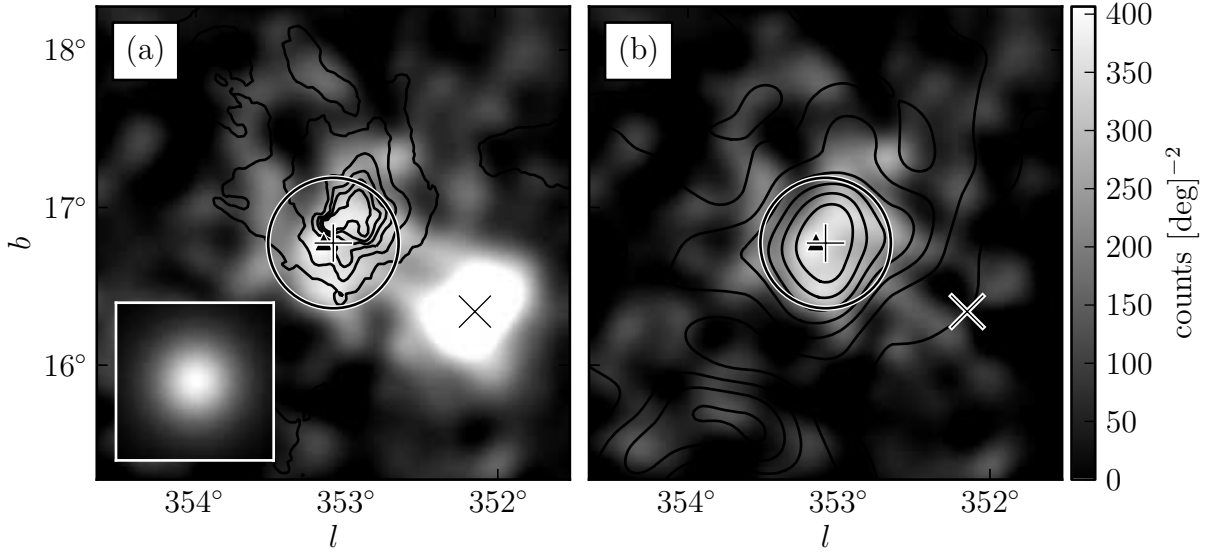


Fig. 11.— A diffuse-emission-subtracted 1-100 GeV counts map of (a) the region around 2FGL J1627.0-2425 smoothed by a  $0.1^\circ$  Gaussian kernel (b) also the emission from the background source 2FGL J1625.7-2526 subtracted. The red star is the 2FGL position of this source. The red cross and circle are the best position and extension of this source assuming a radially symmetric uniform surface brightness. The contours in (a) correspond to the 100 micrometer image observed by IRAS (Young et al. 1986). The contours in (b) correspond to  $^{12}\text{CO}$  ( $J = 1 \rightarrow 0$ ) emission integrated from -8 km/s to 20 km/s. They are from de Geus et al. (1990), were cleaned using the moment-masking technique (Dame 2011), and have been smoothed by a  $0.25^\circ$  Gaussian kernel.

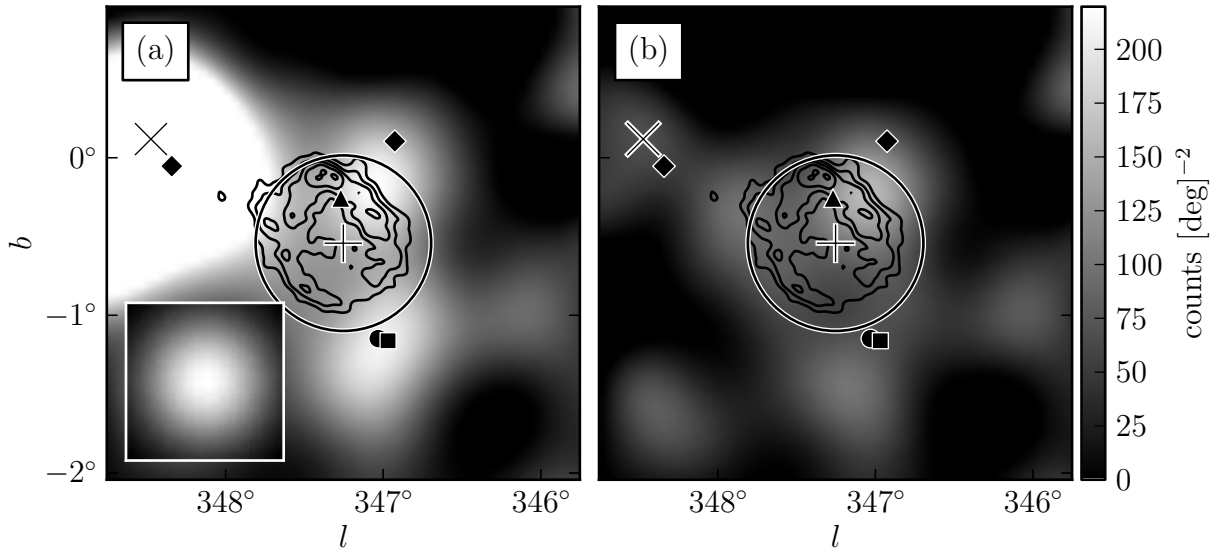


Fig. 12.— A diffuse-emission-subtracted 1-100 GeV counts map of (a) the region around 2FGL J1712.4-3941 smoothed by a 0.25 Gaussian kernel and (b) also the emission from the background sources subtracted. This source is spatially coincident with RX J1713.7-3946 was recently reported by (Abdo et al. 2011c). The light blue contours correspond to the TeV image observed by H.E.S.S. (Aharonian et al. 2007b). The region was analyzed with the same background model as (Abdo et al. 2011c). Source A (blue cross) is spatially coincident with 2FGL J1715.4-4024c (blue star). The gray crosses represent from left to right the position of source B and C which were added to the background model.

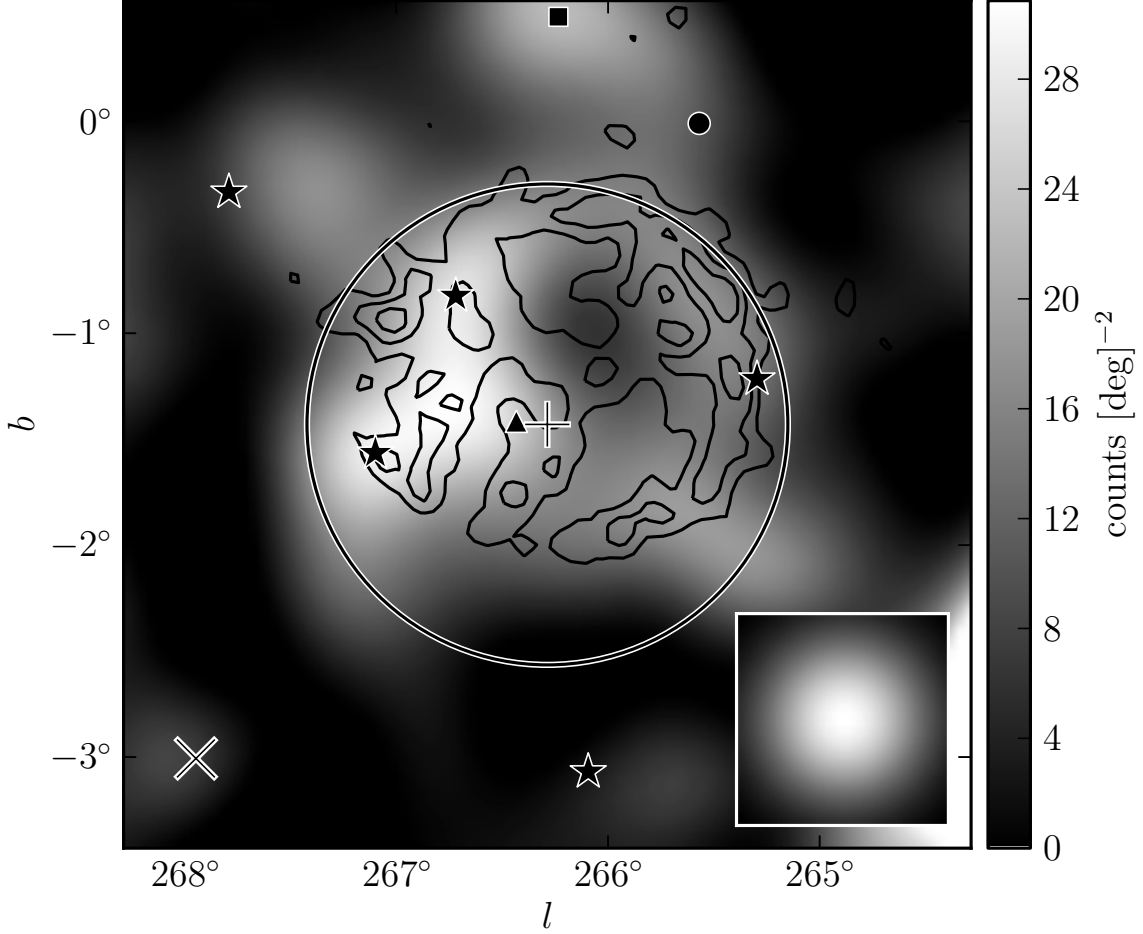


Fig. 13.— A diffuse-emission-subtracted 10-100 GeV counts map of the region around 2FGL J0851.7-4635 smoothed by a  $0.25^\circ$  Gaussian kernel. The red star is the 2FGL position of this source. The red cross and circle are the best fit position and extension of the source assuming a radially symmetric uniform surface brightness. The inner three green stars are (from left to right) 2FGL J0853.5-4711, 2FGL J0855.4-4625, and 2FGL J0848.5-4535 which were removed because they are part of the extended source. The farther away green stars are (from left to right) 2FGL J0901.7-4655 and 2FGL J0858.0-4815 which were removed because they were not significant above 10 GeV. The blue cross is the relocated position of 2FGL J0854.7-4501. This extended source is spatially coincident with the Vela Jr SNR. The light blue contours correspond to the TeV image of Vela Jr. observed by H.E.S.S (Aharonian et al. 2007a).

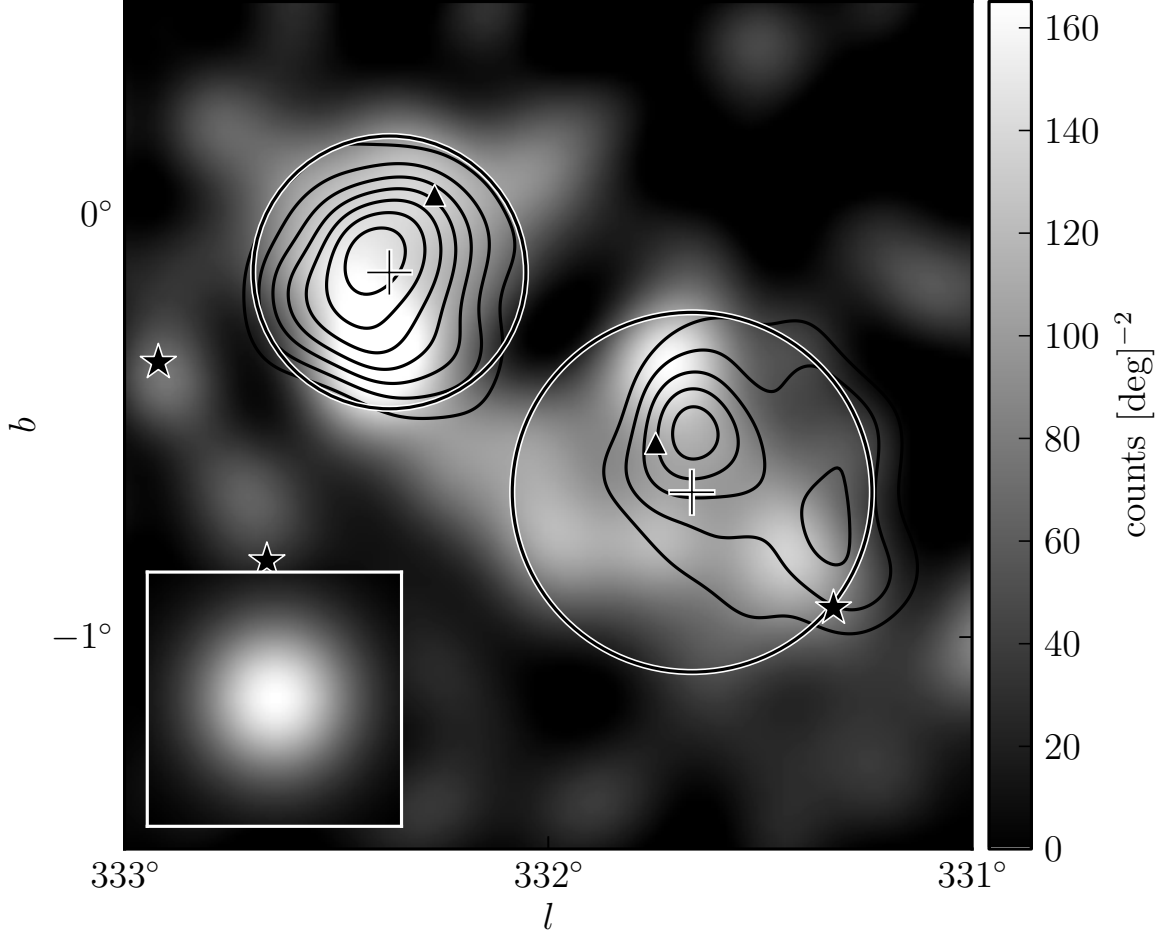


Fig. 14.— A diffuse-emission-subtracted 10-100 GeV counts map of the region around 2FGL J1615.0-5051 (upper left) and 2FGL J1615.2-5138 (lower right) smoothed by a  $0.1^\circ$  Gaussian kernel. The red stars are the catalog positions of these sources. The red stars and circles are the best fit positions and extensions of these sources assuming a radially symmetric uniform surface brightness. The green star inside the extension of 2FGL J1615.2-5138 is 2FGL J1614.9-5212 which was removed because it is part of the extended source. The green stars to the left are 2FGL J1619.7-5040c and 2FGL J1620.6-5111c which were removed because they were not significant above 10GeV. These are shown as green stars. The light blue contours correspond to the TeV image of the extended sources HESS J1616-508 (left) and the extended source HESS J1614-518 (right) observed by H.E.S.S (Aharonian et al. 2006) 2FGL J1615.0-5051 is spatially consistent with HESS J1616-508 and 2FGL J1615.2-5138 is spatially consistent with HESS J1614-518.

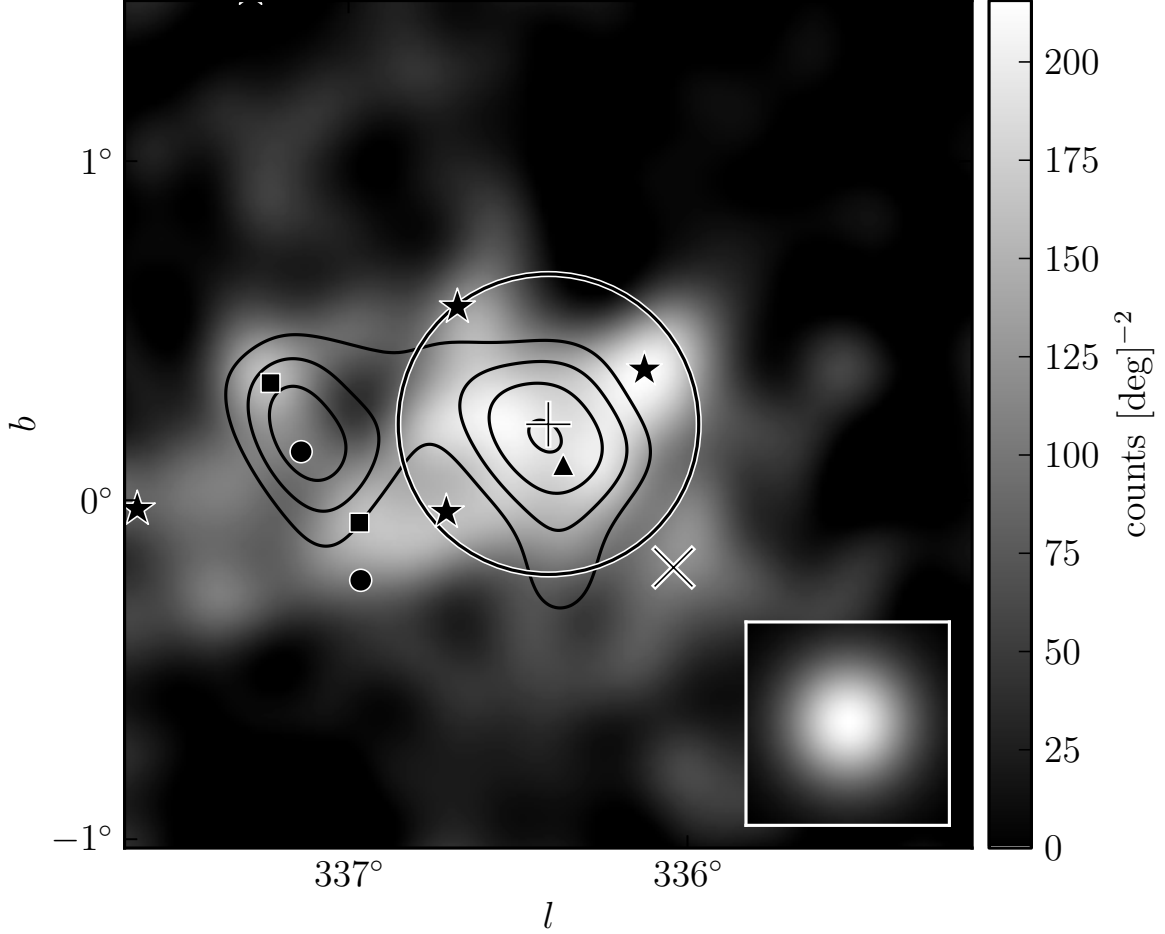


Fig. 15.— A diffuse-emission-subtracted 10-100 GeV counts map of the region around 2FGL J1632.4-4753c smoothed by a  $0.1^\circ$  Gaussian kernel. This source is in a crowded region. The red star is the 2FGL position of this source. The red cross and circle are the best fit position and extension 2FGL J1632.4-4753c assuming a radially symmetric uniform surface brightness. The three green crosses inside the extension are 2FGL J1631.7-4720c, 2FGL J1630.2-4752, and 2FGL J1634.4-4743c.4-4820c which were removed because they are part of the extended source. The blue stars and crosses are the catalog positions and the relocated positions of (from left to right) 2FGL J1635.4-4717c and 2FGL J1636.3-4740c. The farther away green stars are other catalog sources which were removed because they are not significant above 10 GeV. This extended source is spatially coincident with the extended H.E.S.S. source HESS J1632-478. The light blue contours correspond to the TeV image observed by H.E.S.S. (Aharonian et al. 2006).

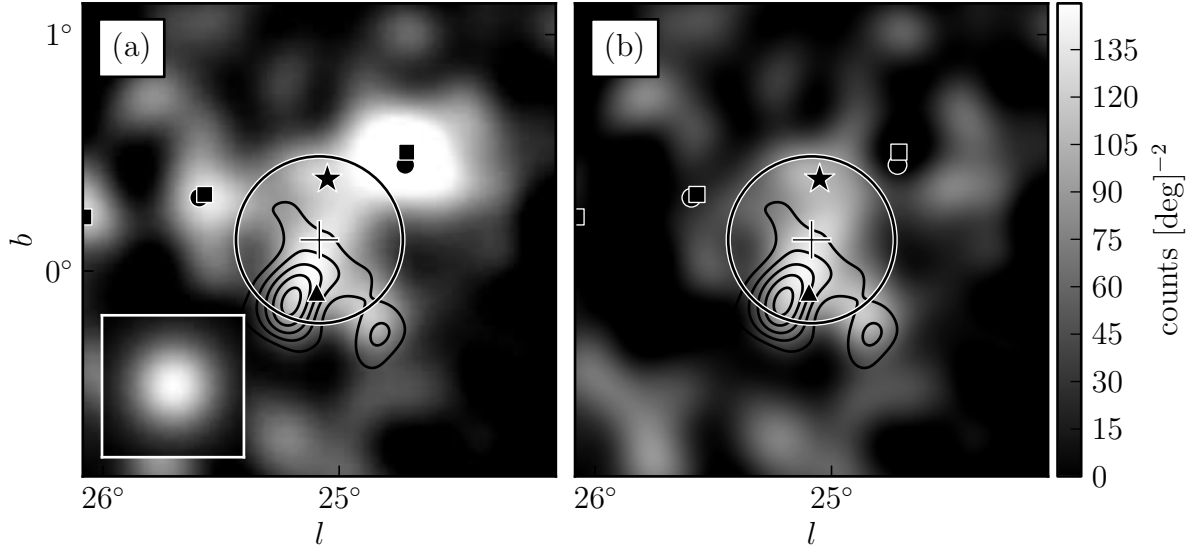


Fig. 16.— A diffuse-emission-subtracted 10-100 GeV counts map of (a) the region around 2FGL J1837.3-0700c smoothed by a  $0.1^\circ$  Gaussian kernel and (b) also the emission from the background sources subtracted. The red star is the 2FGL position of this source. The red cross and circle are the best fit position and extension of 2FGL J1837.3-0700c assuming a radially symmetric uniform surface brightness. The blue stars and crosses are the catalog position and the relocated position of (from left to right) 2FGL J1839.3-0558c, 2FGL J1836.8-0623c, and 2FGL J1834.7-0705c. The green cross inside the extension is 2FGL J1835.5-0649 which was removed because it is part of the extended source. The farther away green star is 2FGL J1839.0-0539 which was removed because it is not significant above 10 GeV. This source is spatially coincident with the TeV source HESS J1837-069. The light blue contours correspond to the TeV image observed by H.E.S.S. (Aharonian et al. 2006).

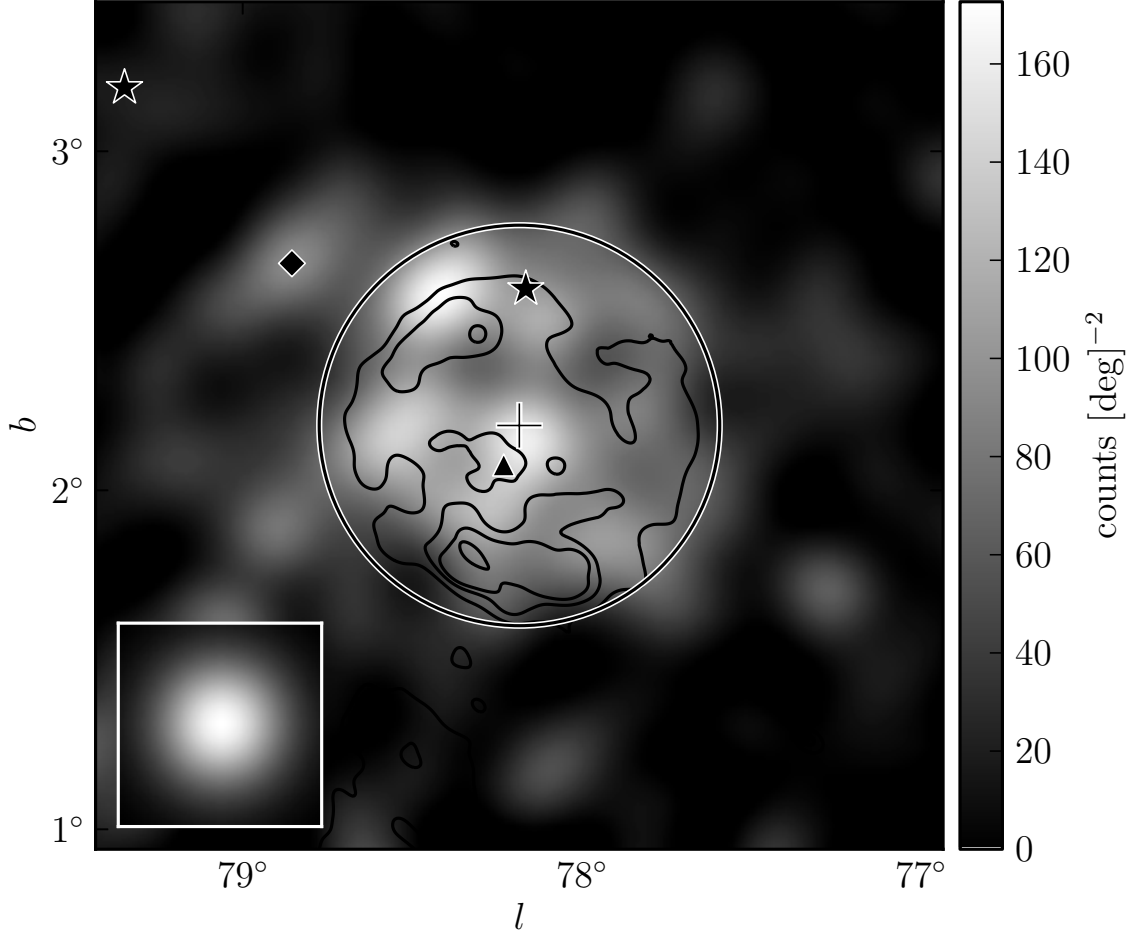


Fig. 17.— A Diffuse subtracted 10 GeV to 100 GeV counts map of the region around 2FGL J2021.5+4026 smoothed by a  $0.1^\circ$  Gaussian kernel. The triangle (colored red in the online version) represents the 2FGL position of 2FGL J2021.5+4026. The plus and circle (colored red) represent the best fit position and extension 2FGL J2021.5+4026 assuming a radially symmetric uniform surface brightness. The star (colored green) inside the extension represents the position of 2FGL J2019.1+4040 which was removed because it is part of the extended source. The diamond (colored purple) is the position a source not in the two year catalog which was added to the region. 2FGL J2021.5+4026 is spatially coincident with the  $\gamma$  Cygni SNR. The contours (colored light blue) correspond to the 408MHz image of  $\gamma$  Cygni observed by the Canadian Galactic Plane Survey.



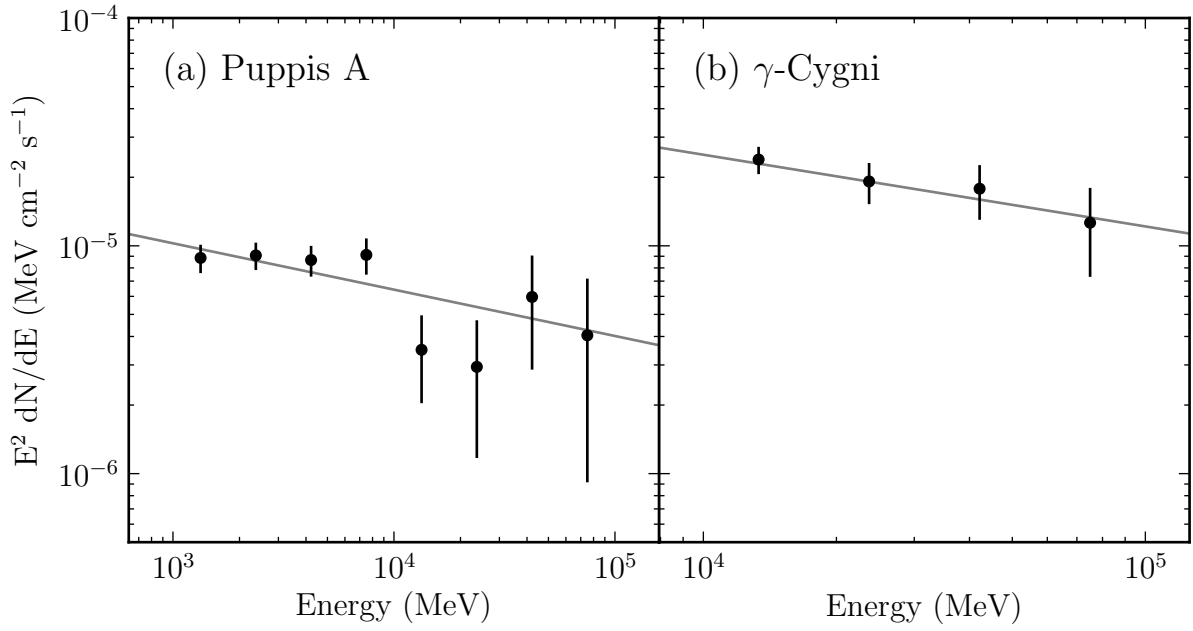


Fig. 18.— The spectral energy distribution of the extended sources Puppis A (2FGL J0823.0-4246) and  $\gamma$ -Cygni (2FGL J2021.5+4026). The lines (colored red in the online version) are the best fit power-law spectral model of these sources. The LAT spectral errors are statistical only.

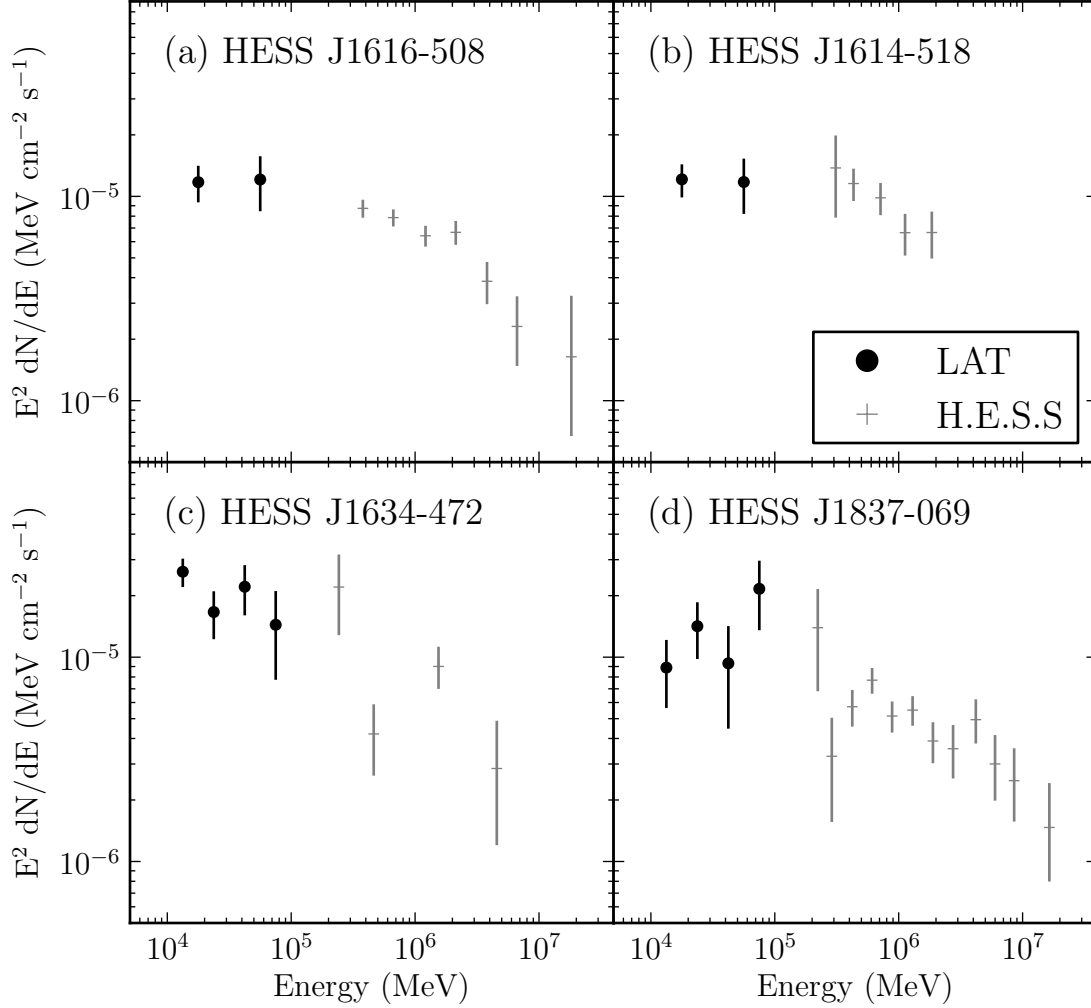


Fig. 19.— The spectral energy distribution of four the extended sources associated with extended TeV sources. The black points with circular markers are the LAT data points. The points with dashed markers (colored red in the electronic version) are the H.E.S.S. points of the associated sources. Plot (a) shows the GeV SED of 2FGL J1615.0-5051 together with the TeV SED of HESS J1616-508. Plot (b) shows 2FGL J1615.2-5138 and HESS J1614-518 Plot (c) shows 2FGL J1632.4-4753c and HESS J1632-478. Plot (d) shows 2FGL J1837.3-0700c and HESS J1837-069. The H.E.S.S. data points are from (Aharonian et al. 2006) Both LAT and H.E.S.S. spectral errors are statistical only.

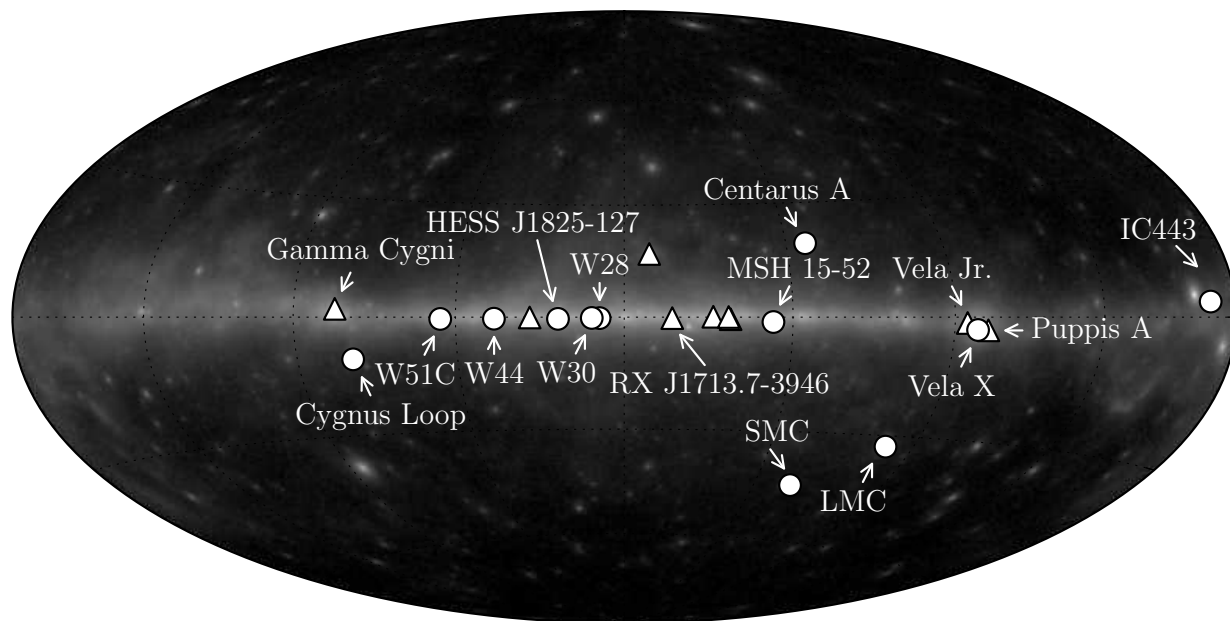


Fig. 20.— A plot of all GeV extended sources detected by the LAT with two years of data. The twelve extended sources included in 2FGL are indicated by the circular markers (colored red in the online version). The nine new extended sources analyzed in this paper are the triangular markers (colored orange in the online version).

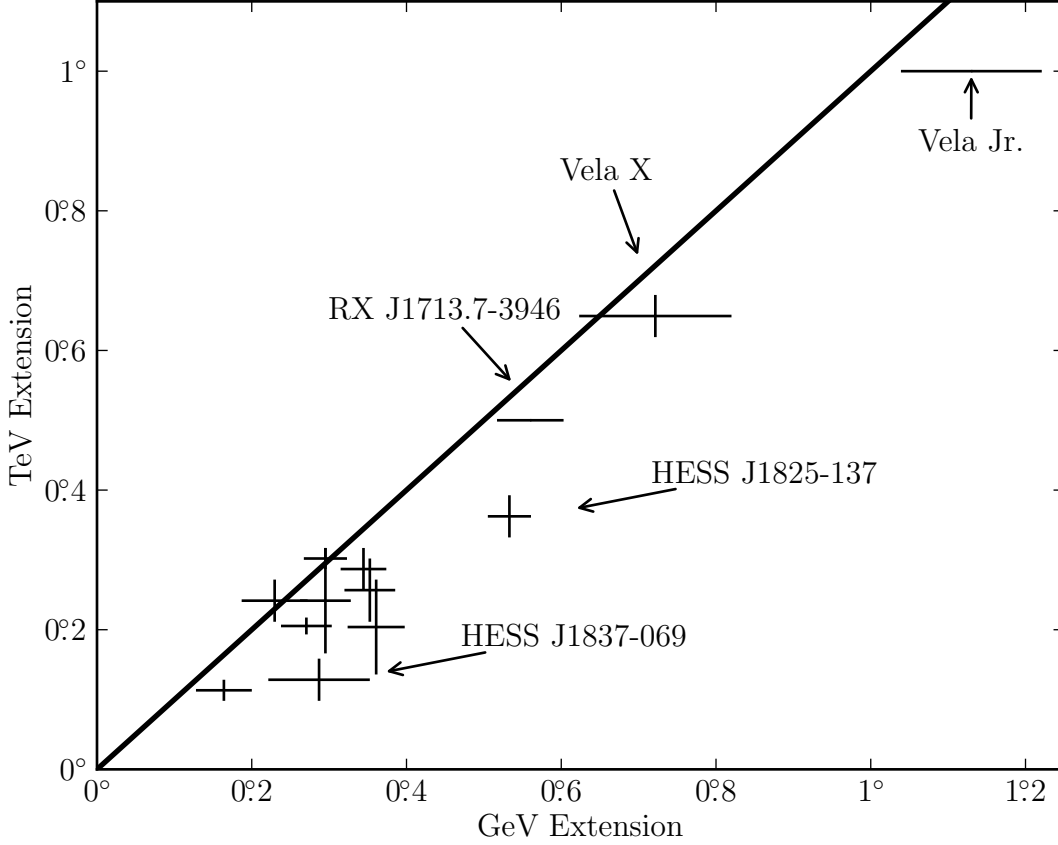


Fig. 21.— A comparison of the GeV and TeV sizes of LAT extended sources detected by TeV instruments. The TeV extensions of W30, 2FGL J1837.3-0700c, 2FGL J1632.4-4753c, 2FGL J1615.0-5051, and 2FGL J1615.2-5138 (Aharonian et al. 2006). The TeV extensions of MSH 15-52, HESS J1825-137, Vela X, Vela Jr., RX J1713.7-3946 and W28 are from (Aharonian et al. 2005, 2006b,c, 2007a,b, 2008). The TeV extension of IC443 is from (Acciari et al. 2009) and W51c is from (Krause et al. 2011). The LAT extension of Vela X is from (The Fermi LAT Collaboration & Timing Consortium 2010). Except for RX J1713.7-3946 Vela Jr., the TeV sources were fit assuming a Gaussian surface brightness so the plotted GeV and TeV extensions were first converted to  $r_{68}$  (see Section 2.5). Because of their large size, the shape of RX J1713.7-3946 and Vela Jr. were not directly fit in TeV. Here, we take their sizes to be the same as the LAT size and do not converted it to  $r_{68}$ . The LAT extension errors are the statistical and systematic errors added in quadrature. The TeV size of MSH 15-52, HESS J1614-518, HESS J1632-478, and HESS J1837-069 have only been reported with an elliptical Gaussian fit and so the plotted size is the average of semi-major and semi-minor axis.

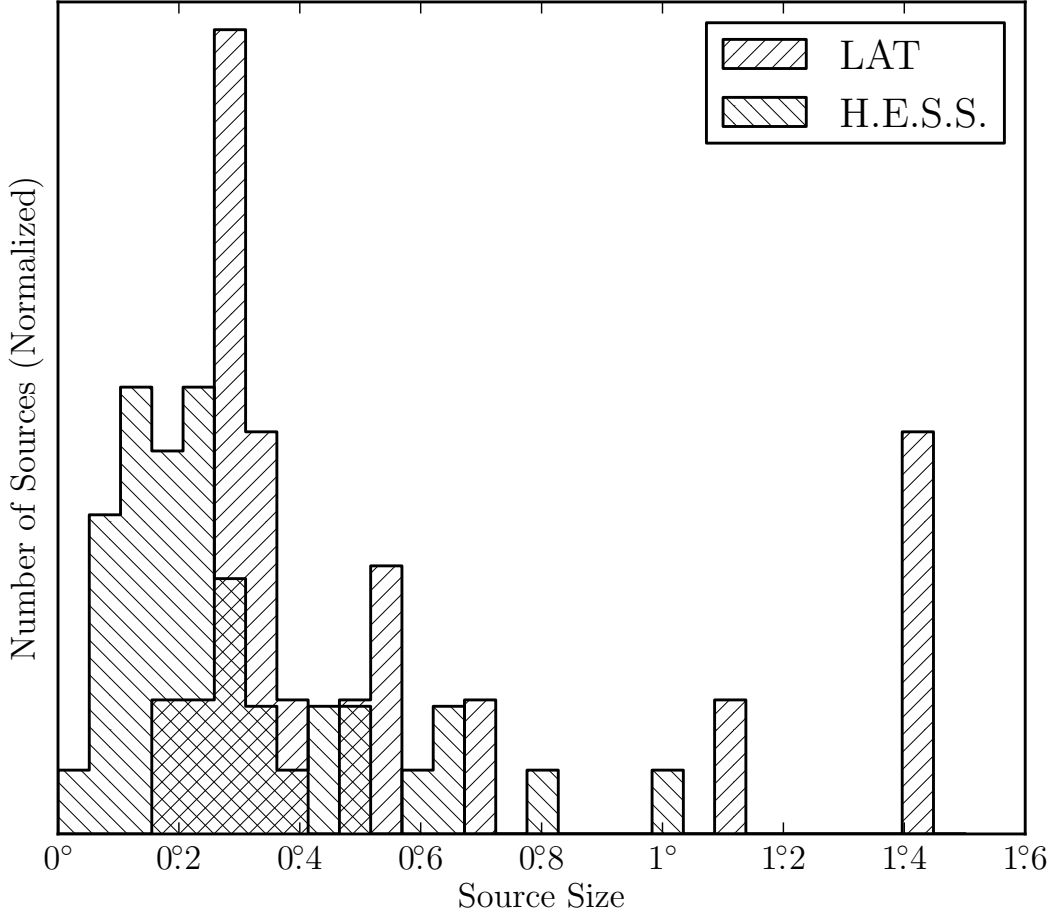


Fig. 22.— The distribution of the GeV size of the 22 extended LAT sources (colored blue in the electronic version) and the TeV size of the 42 extended H.E.S.S. sources (colored red in the electronic version). The extension of the LAT sources comes from Table 3, Table 4, and from The Fermi LAT Collaboration & Timing Consortium (2010). The TeV extension of the 42 extended H.E.S.S. sources comes from the H.E.S.S. Source Catalog (The H.E.S.S. Collaboration 2011). Except for RX J1713.7-3946 and Vela Jr., the H.E.S.S. sources were fit with a Gaussian surface brightness model and so the LAT and H.E.S.S. sizes are first converted to  $r_{68}$ . (see Section 2.5). Because the spatial morphology of RX J1713.7-3946 and Vela Jr. is poorly matched by a Gaussian surface brightness model, the GeV and TeV extensions are included assuming a uniform surface brightness.

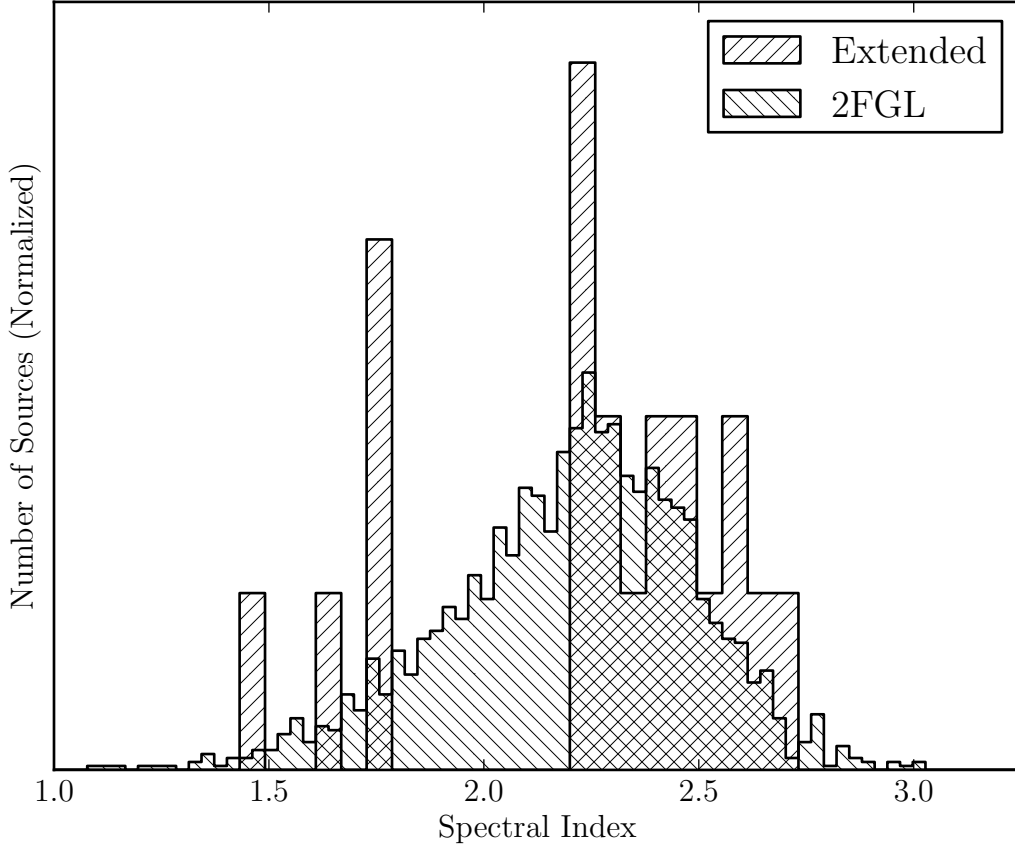


Fig. 23.— The distribution of spectral indices of all 1873 2FGL sources (colored red in the electronic version) and the spatially extended sources (colored blue in the electronic version). The spectral indices of LAT extended sources are taken from Table 3 and 4. The index of Centarus A is taken to be 2.58 from Abdo et al. (2011b) and the index of Vela X is taken to be 2.41 from The Fermi LAT Collaboration & Timing Consortium (2010).